RESEARCH ARTICLE

NANO · MICRO small
www.small-journal.com

A Dual-Mode On-Chip 3D-Printed Nanoengineered Platform for Extraction and Electrochemical Detection of Enrofloxacin

*Supratim Mahapatra, Ankur Singh, Ratul Paul, and Pranjal Chandra**

A magnetic molecularly imprinted polymer (MMIP) is synthesized for the development of a highly selective and sensitive electrochemical sensing platform targeting enrofloxacin (ENF). The micro-sized mesoporous core-shell MMIP structure is constructed with a magnetite core and an outer shell functionalized using 3-aminopropyltriethoxysilane (APTES) as the monomer. The synthesis is optimized and validated using a range of physical and electrochemical techniques. The sensor is designed with dual-mode functionality, integrating magnetic separation for efficient target extraction and electrochemical detection for precise quantification. A conventional electrode is modulated with multi-layer nano-functionalization to improve its analytical performance, while 3D-printed components ensure miniaturization, fabrication precision, and scalability. The resulting device exhibits a broad linear detection range from 100 pM to 10 mM (10^{-10} to 10^{-2} M), with an exceptionally low limit of detection (LOD) of 161 fM (1.61×10^{-13} M). As ENF is recurrently administered to cattle, milk is used as a real sample to demonstrate the sensor's proof-of-application. Real sample analysis showed a high recovery rate (90.23% to 97.29%) with minimal matrix interference, confirming reliability in complex biological matrices. The platform demonstrates exceptional reproducibility and stability, offering a robust and scalable solution for environmental and food safety monitoring.

1. Introduction

Magnetic core-shell microparticles are extensively researched due to their properties of easy separation and manipulation using external magnetic fields.[1] These particles typically consist of a magnetic core, which provides the essential magnetic properties for quick and efficient separation, and a customizable shell that can be tailored for specific functionalities. The shell, often made of materials like silica, polymers, or other functional coatings, serves as a versatile platform for applications such as selective binding, catalysis, and biocompatibility. This adaptability makes them highly desirable in fields like sensing, bioimaging, drug delivery, energy storage, and environmental remediation.[2–5]

One particularly promising application of these core-shell structures lies in their use as substrates for creating highly selective binding materials. By combining their magnetic properties with advanced surface engineering, researchers have developed innovative platforms for synthesizing materials capable of recognizing and binding specific target molecules.[6] For example, molecularly imprinted polymers (MIPs) are synthetic polymers designed to have specific binding sites that mimic the behavior of natural receptors, offering high selectivity and affinity for target molecules. The integration of magnetic cores into MIPs enhances their functionality significantly. These magnetically responsive MIPs, often referred to as MMIPs, that are particularly advantageous for their distinctive characteristics to present high active surface area and ease of separation. The shell surrounding the core not only protects the magnetic material but also provides a foundation for the imprinting process, which can be further modified to improve binding performance.

In this study, we developed an MMIP using magnetite nanoparticles (NPs) as a magnetic core, specifically functionalized with an outer shell composed of APTES, to detect an antibiotic ENF. Magnetite, an inverse spinel ferrite, was selected due to its intrinsic strong magnetic properties, enabling efficient magnetic separation and easy manipulation. Conventional magnetite NPs suffer from aggregation, poor dispersibility in aqueous media, limited chemical stability, and limited surface functionality.[7] Compared to this, our APTES-functionalized core-shell magnetite notably mitigates these drawbacks. The tailored APTES-based shell optimizes the molecular imprinting process, thus significantly enhancing the selectivity and efficiency of the resultant MMIP. Magnetite possesses a characteristic crystal structure with a cubic close-packed arrangement of oxygen ions, where Fe^{3+} ions occupy tetrahedral sites, and Fe^{2+} and Fe^{3+} ions are distributed across octahedral sites.[8] This structural arrangement is responsible for its ferrimagnetic behavior, as the magnetic moments of Fe ions in the tetrahedral and octahedral sites align oppositely, resulting in a net magnetic moment. Consequently, at room temperature, magnetite displays robust magnetism and finds extensive applications in magnetic storage devices and

S. Mahapatra, A. Singh, R. Paul, P. Chandra
Laboratory of Bio-physio Sensors and Nanobioengineering
School of Biochemical Engineering
Indian Institute of Technology (BHU) Varanasi
Varanasi, Uttar Pradesh 221005, India
E-mail: pranjal.bce@iitbhu.ac.in

The ORCID identification number(s) for the author(s) of this article can be found under https://doi.org/10.1002/smll.202502880

DOI: 10.1002/smll.202502880

biomedical fields.[9] Utilizing APTES as the functional monomer for the shell formation provides several distinctive advantages. APTES, a well-known silane coupling agent, introduces amine ($-NH_2$) functionalities onto nanoparticle surfaces, significantly enhancing their reactivity and versatility.[10] These amine functionalities act as reactive sites for subsequent modifications, facilitating the conjugation of diverse biomolecules, catalysts, or additional functional layers crucial for targeted drug delivery, biosensing, and environmental remediation. Furthermore, APTES functionalization markedly improves particle stability and dispersibility in aqueous environments, preventing undesirable aggregation and ensuring uniform performance. The robust covalent bonding capability of APTES with silica-based shells also considerably strengthens the structural integrity of the core-shell microparticles, enhancing durability under harsh operational conditions. By strategically integrating the superior magnetic properties of magnetite and the functional versatility imparted by APTES, we successfully designed an MMIP structure capable of precise molecular recognition. This engineered platform provides robust dual-mode functionality, combining efficient magnetic separation with selective electrochemical detection of ENF.

Particularly for treating bacterial infections in cattle, ENF, a fluoroquinolone antibiotic, is routinely used in veterinary medicine. It is a vital medication for maintaining cattle health as its broad-spectrum antibacterial action against Gram-negative and Gram-positive pathogens ensures to prevention and treatment of respiratory infections, intestinal illnesses, and mastitis.[11] This, in turn, improves general production and reduces economic losses in the dairy and meat sectors. However, the non-administered use of ENF brings serious questions about public health and food safety.[12] If withdrawal times are not precisely followed, residual ENF and its metabolites can remain in animal-derived goods, including milk and meat. Even in minute quantities, these residues help antibiotic-resistant bacteria to arise, eventually endangering human health. Maximum residual limits (MRLs) for ENF in food items have been regulated at 2.78×10^{-7} M, according to the commission report of the European Union .[13] Thus, guaranteeing food safety compliance depends on the development of sensitive and accurate analytical techniques for ENF residue detection.

Various sophisticated analytical techniques for the quantification of ENF have been well established, which include capillary electrophoresis (CE), liquid chromatography, liquid chromatography-tandem mass spectroscopy (LC-MS), fluorescence, and immunoassay, etc.[14–17] Although these approaches have been considered gold standard techniques, there are limitations too, that mark expensive instrumentation, high maintenance cost, tedious and complex sample preparation, requirement of skilled operators, and time-consuming. Therefore, the establishment of a simple, fast, sensitive, accurate, and economical approach was of great requirement for the detection of ENF. Electrochemical sensors have emerged as a powerful tool for sensing pharmaceutical residues, owing to their inherent advantages, including high sensitivity, high selectivity, affordability, and quick response time.[18–20] Previously, several electrochemical approaches, including voltammetric and amperometric sensors, have also been reported for ENF detection.[21,22] However, these methods often face critical limitations associated with sensitivity or biological interferents in complex food matrices that affect signal accuracy significantly. Additionally, electrode fouling caused by ENF adsorption and sample impurities reduces sensor stability and operational lifespan.[23] Most existing sensors also require extensive sample preparation and pre-treatment, limiting their practical application for routine monitoring. Furthermore, achieving ultra-low detection limits that comply with regulatory thresholds remains a challenge for many conventional electrochemical sensors.[24]

In this study, we presented a highly selective and portable on-chip electrochemical sensing platform designed for the detection of ENF, addressing the critical need for real-time monitoring of antibiotic residues in food safety applications. Our innovative approach integrates a miniaturized, custom 3D-printed electrochemical sensing device (**Scheme 1**) with advanced technologies, including molecular imprinting, magnetic separation, and nanomaterial-enhanced electrochemical transduction, to achieve rapid and precise detection. At the base of this platform is the bifunctional MMIP, which serves as the key recognition element, enabling selective binding of ENF while facilitating magnetic-assisted separation for enhanced efficiency. The electrode surface is engineered with gold nanoparticles (AuNPs) and reduced graphene oxide (rGO), which significantly enhance electron transfer, increase surface area, and improve stability.[25–28] The incorporation of AuNPs and rGO is pivotal in boosting the sensor's signal response and conductivity, ensuring high sensitivity and reliability.[29,30] By synergistically combining molecular imprinting, magnetic-assisted separation, and nanomaterial-enhanced electrochemistry, this on-chip platform offers a cost-effective, user-friendly, and scalable solution for on-site antibiotic detection. Its versatility makes it a promising tool for a wide range of applications, including food safety monitoring, pharmaceutical screening, and environmental surveillance. The major advantage of this study lies in the integration of efficient magnetic separation with sensitive electrochemical detection, coupled with the development of miniaturized equipment enabled by advanced additive manufacturing. Traditional electrochemical sensors for antibiotic detection typically require complex pre-treatment processes, suffer from electrode fouling, and lack portability. In contrast, our platform employs an MMIP that not only selectively recognizes and isolates ENF from complex samples but also allows rapid and straightforward separation under an external magnetic field. Moreover, the incorporation of a miniaturized 3D-printed sensing device significantly reduces sample and reagent volumes, enabling rapid, cost-effective, and on-site detection. This miniaturization further enhances the platform's practicality for real-time food safety and environmental monitoring applications, addressing critical limitations associated with conventional laboratory-bound analytical methods.

2. Results and Discussion

2.1. Synthesis and Characterization of the MMIP and MNIP

Scheme 2A shows the detailed synthesis steps of the MMIP, where ENF was chosen as the template molecule, TEOS as the crosslinker, and APTES as the functional monomer. At first, ENF and APTES created pre-polymer complexes by forming hydrogen bonds and electrostatic interactions between the amine groups in APTES to the carboxyl and ketone groups in ENF. Thereafter,

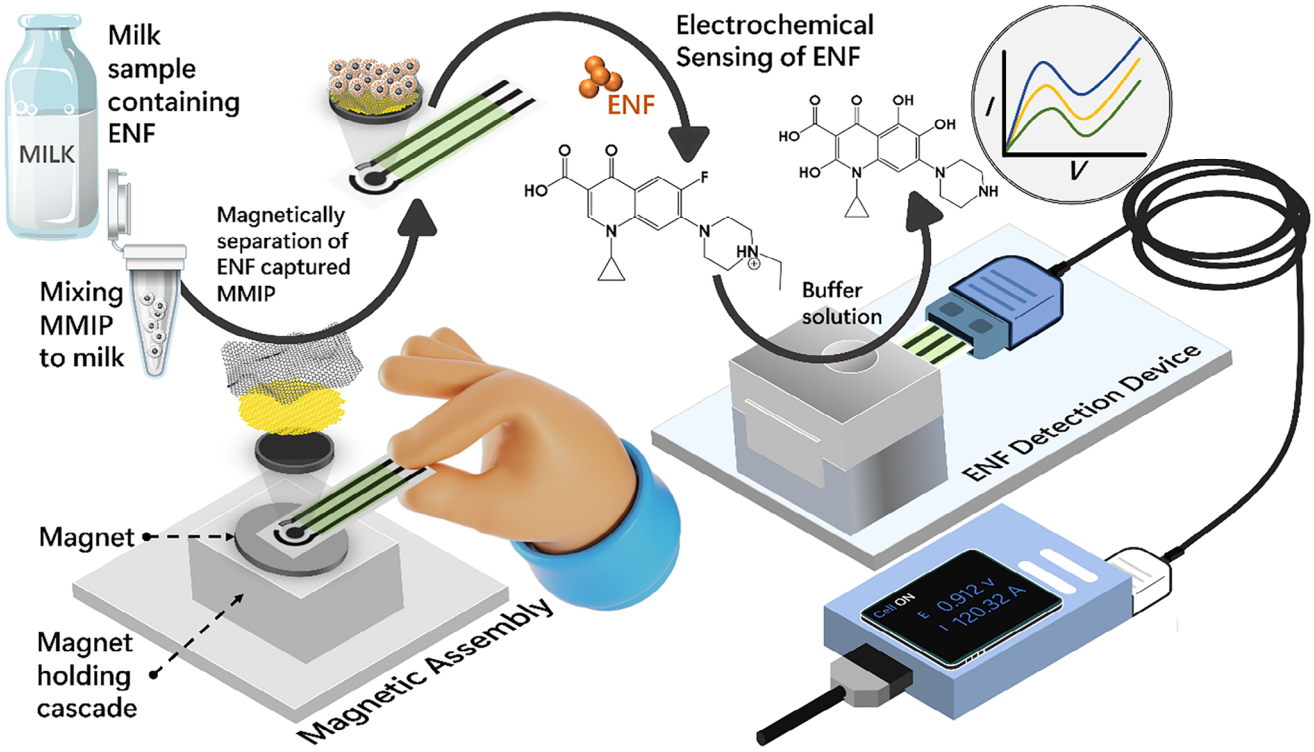

Scheme 1. Schematic representation of the fabricated electrochemical sensing platform for ENF detection. The process involves sequential modification of the working electrode with AuNPs and rGO, followed by the application of the MMIP microparticles for selective ENF recognition.

the negatively charged magnetite NPs were evenly dispersed in a mixture of ethanol and water by using sonication. The addition of $NH_3 \bullet H_2O$ to the solution introduces NH_4^+ ions that get absorbed on the surface of the magnetite NPs, eventually forming a positively charged layer. The addition of $NH_3 \bullet H_2O$ also hydrolyzes TEOS, which helps create a layer of silica network around the magnetite NPs. The hydrolyzed TEOS and the prepolymer complex were then combined on the surface of magnetite NPs. This created a magnetic polymer shell that has a 3D network design. Finally, the template molecule (ENF) was taken out from the polymer shell, creating identical spaces that were of the same size and shape as ENF, and also bearing the constant functional groups to bind ENF.

A mixture of ethanol and water was chosen because ENF dissolves well in ethanol, and the reaction between APTES and TEOS works well in blends of alcohol and water.[31] In multiple iterations, we found that using a 2:1 ratio of ethanol to water resulted in an evenly distributed MIP shell with minimum aggregation, creating a solid and well-mixed polymer structure. According to the Stöber process, $NH_3 \bullet H_2O$ works as a catalyst and affects how quickly TEOS breaks down into polymers, and it also impacts the thickness of the MIP shell.[32] The thickness of the MIP shell increases with higher $NH_3 \bullet H_2O$ concentration due to accelerated polymerization, while lower concentrations yield thinner, more uniform coatings with better imprinting fidelity (Figure S1, Supporting Information). Thus, using the optimized quantity of $NH_3 \bullet H_2O$ is also being tested. A volume of 5 mL of $NH_3 \bullet H_2O$ created a smooth MIP shell that is ≈ 53 nm thick. This thickness helps the material quickly absorb substances while keeping its consistent shape. The ratio of the template molecule (ENF) to the functional monomer (APTES) is important for how well the MIP can absorb substances and how selectively it can do so. Using too many functional monomers can create binding sites that aren't specific, while using too few can cause partial imprinting. After a thorough study, it was found that a molar ratio of 100 mM of ENF to 2 mL of APTES provides an advantage for wide analytical assessment.

2.1.1. Surface Morphology Analysis

SEM analysis was performed to infer the morphology and shape of the developed MMIP and MNIP. **Figure** 1A–C shows a well-defined spherical surface morphology of the synthesized MMIP particles with an average diameter of ≈522 nm. A similar observation was made in the case of MNIP microparticles as well (Figure S2A–B). The observed spherical shape can be attributed to the thermodynamic preference for minimizing surface energy, as it offers the lowest surface-to-volume ratio, leading to energetically stable particles. The homogeneous nucleation and controlled growth during the coprecipitation process played a crucial role in maintaining this morphology. Additionally, the presence of APTES and TEOS facilitated the uniform deposition of the polymer shell over the magnetite core, preventing aggregation and ensuring smooth particle formation. Furthermore, the electrostatic repulsion among functionalized particles and magnetic interactions helped maintain particle stability. The spherical morphology of MMIP and MNIP particles confirms their

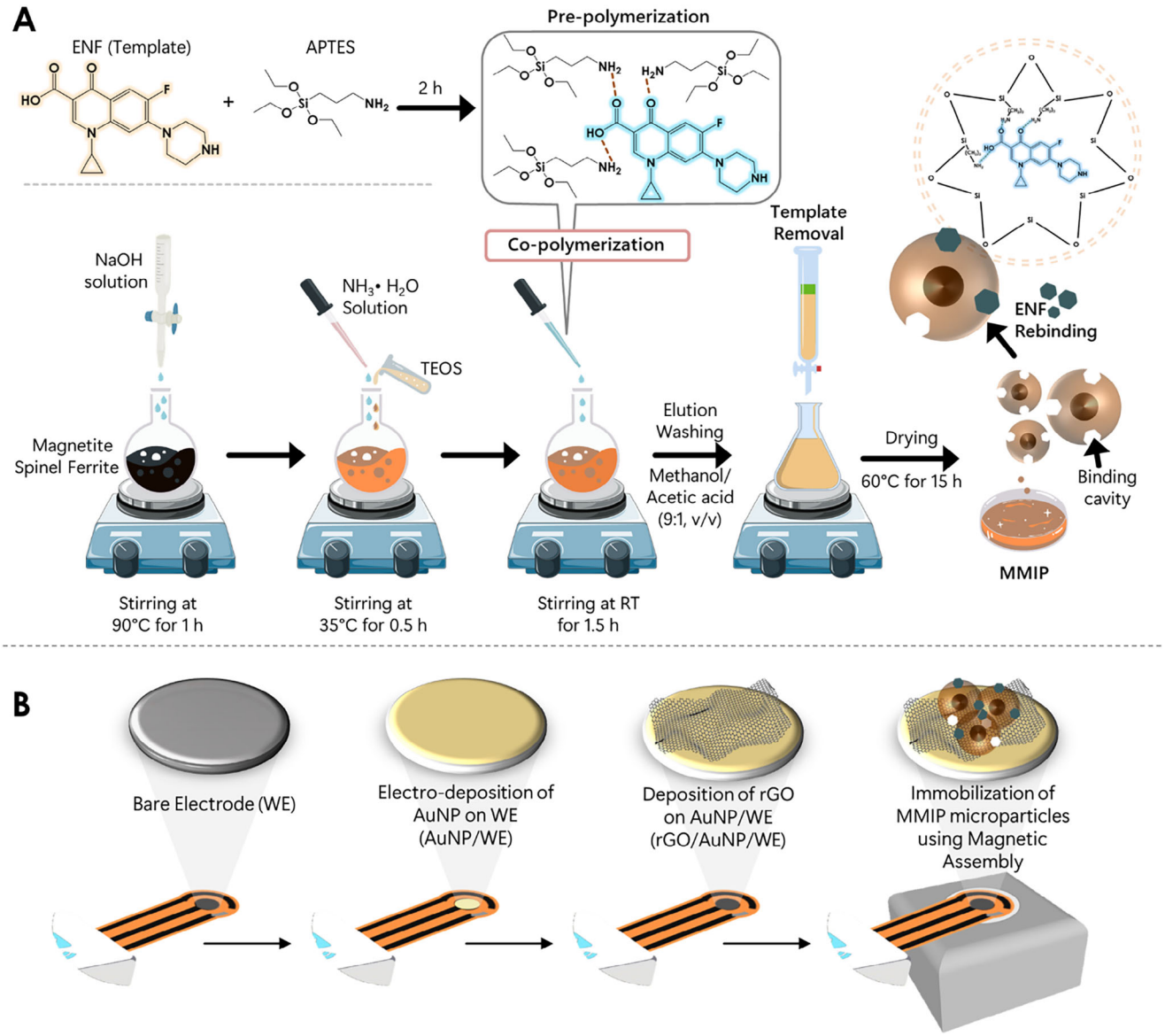

Scheme 2. Schematic representation of the synthesis and fabrication process of the MMIP-based electrochemical sensor for enrofloxacin (ENF) detection. A) Stepwise synthesis of MMIP, including magnetite core formation, surface functionalization with APTES, polymerization with TEOS, and template removal to create selective ENF binding cavities. B) Fabrication of the sensing electrode, involving electrodeposition of gold nanoparticles (AuNPs), coating with reduced graphene oxide (rGO), and final modification with MMIP to develop the MMIP/rGO/AuNP/WE sensing probe.

well-optimized synthesis conditions, leading to a structurally stable and reproducible polymeric architecture. Further, the particle size distribution analysis was performed using ImageJ software, showing the Gaussian distribution of the MMIP microparticles (Figure 1C inset).

TEM analysis was conducted to confirm the structural integrity and core-shell architecture of the synthesized MMIP (Figure 1D–F) and MNIP microparticles (Figure S2C–D). TEM images offered a comprehensive visualization of the magnetite core and its surrounding polymeric shell, demonstrating a clearly defined core-shell morphology for both MMIP and MNIP. The silane-coated polymeric shell was distinctly observable, confirming the effective functionalization of magnetite NPs with APTES and TEOS. The diameter of the MMIP particles was measured to be between 520–550 nm (Figure 1F), consistent with the SEM findings. The TEM images display the magnetite core (darker region) and the outer imprinted polymeric shell (lighter region), with a shell thickness of ≈53 nm designed for ENF recognition through specific binding sites. A similar observation was made in the case of MNIP, with the non-imprinted polymeric shell uniformly encapsulating the magnetic core. The consistent thickness of the polymer shells in both MMIP and MNIP indicates effective surface modification, facilitating selective binding in MMIP and maintaining the structural integrity of the particles. These findings complement the SEM observations and confirm the successful fabrication of the MMIP and MNIP

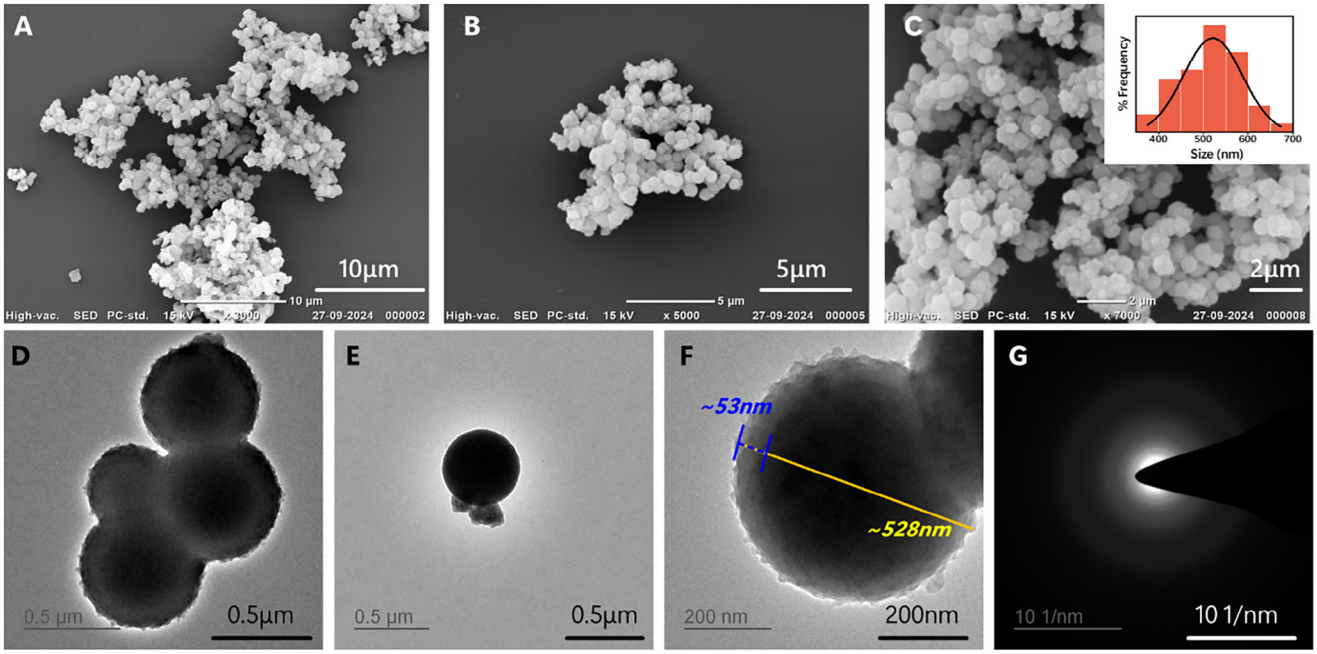

Figure 1. Microscopic characterization of the synthesized MMIP. A–C) SEM images at different magnifications showing the spherical morphology and uniform distribution of MMIP microparticles. The inset in(C) presents the particle size distribution. D–F) TEM images illustrating the core-shell architecture of MMIP, where the dark region represents the magnetite core and the lighter region corresponds to the imprinted polymer shell. The uniform polymeric shell (≈53 nm thick) demonstrates successful molecular imprinting, ensuring selective recognition of ENF. G) SAED pattern obtained for the MMIP microparticle.

microstructures, presenting them as viable candidates for further electrochemical sensing applications.

Figure 1E and Figure S2E represent the selected area electron diffraction (SAED) patterns obtained for the MMIP and MNIP microstructures, respectively. In both cases, a characteristic diffuse halo was observed, confirming the amorphous nature of the polymeric shell. The absence of well-defined diffraction spots or sharp rings indicates that the outer shell, primarily composed of APTES-derived polymeric material, lacks long-range crystallinity. This observation aligns with the formation of a silica-based organic–inorganic hybrid network, where the polymerization of APTES results in a crosslinked, yet non-crystalline, structure encapsulating the magnetic core. Although the core of the MMIP and MNIP consists of magnetite, which typically exhibits crystalline diffraction rings, the SAED pattern is dominated by the amorphous polymeric shell. This suggests that the polymeric shell effectively masks the diffraction signature of the underlying magnetite, confirming the successful encapsulation of the magnetic core within the amorphous APTES-based matrix. This encapsulation is critical for stabilizing the molecularly imprinted and non-imprinted structures and ensuring their functionality. The amorphous nature of the polymeric shell is particularly advantageous for molecular imprinting applications, as it facilitates a homogeneous distribution of binding sites, free from the influence of crystalline grain boundaries, which could otherwise disrupt the uniformity of the imprinted cavities. This structural disorder enhances surface accessibility and molecular recognition capabilities, ensuring high specificity for the target analyte in the case of MMIP. Additionally, the non-crystalline nature of the polymeric matrix minimizes interference from diffraction artifacts, which could compromise the accuracy and specificity of analyte interactions in sensing applications.

2.1.2. XPS Analysis

To further investigate the elemental composition and successful synthesis of the MMIP and MNIP microparticles, X-ray Photoelectron Spectroscopy (XPS) analysis was performed (**Figure 2A**). The XPS spectra confirmed the presence of iron (Fe) and oxygen (O) elements in the magnetite core, as illustrated in Figure 2A (black trace). For the MNIP (blue trace) and MMIP (red trace) microparticles, peaks corresponding to silicon (Si) and nitrogen (N), primarily originating from the functionalization with TEOS and APTES, were observed. However, the peaks associated with the magnetite core were not noted in this case, as XPS is a surface-sensitive technique.

The Fe 2p deconvolution spectrum (Figure 2B) of the magnetite particle revealed two distinct peaks at 709.7 and 723.8 eV, corresponding to Fe $2p_{3/2,}$ and Fe $2p_{1/2}$, respectively. These peaks indicate the Fe^{3+} oxidation state characteristic of the inverse spinel ferrites.[33] The detailed Si 2p spectrum (Figure 2C) associated to the MMIP displayed two peaks at 101.8 and 102.5 eV, attributed to Si–C and Si–O groups, respectively, confirming the silane functionalization on the magnetite surface.[34] Notably, the concentrations of C and O elements increase significantly in the MMIP spectrum compared to the magnetite NPs (Figure S3A), further validating the emergence of polymeric moieties. The C 1s spectrum (Figure S3B) exhibited three distinct peaks at 284.4 eV, 285.4 eV, and 288.0 eV, corresponding to C—Si,

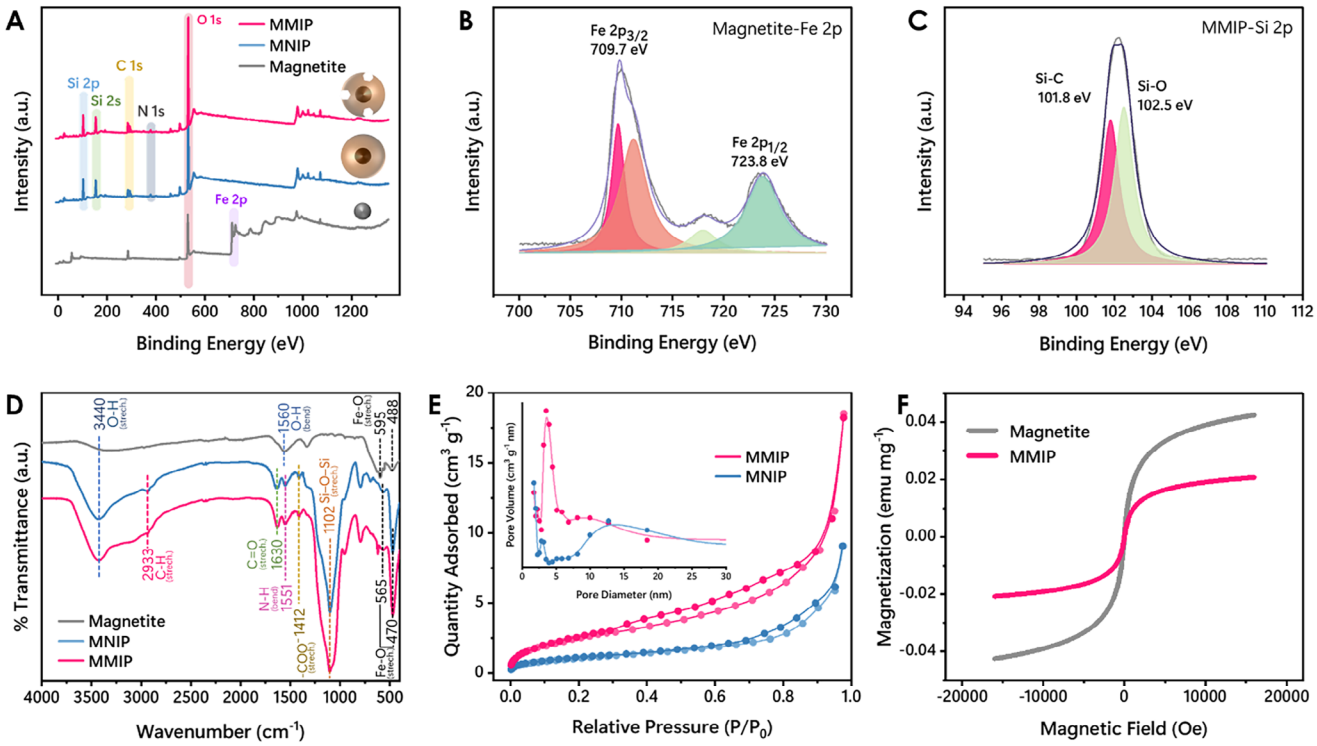

Figure 2. Physicochemical and magnetic characterization of magnetite and MMIP microparticles. A) X-ray photoelectron spectroscopy (XPS) survey spectra of magnetite and MMIP, demonstrating the existence of Fe, O, C, N, and Si elements. B) High-resolution XPS spectra of Fe 2p for magnetite particle. and C) High-resolution XPS spectra of Si 2p for the MMIP microparticles, illustrating functional group alterations following polymerization. D) FTIR spectra of magnetite, MNIP, and MMIP exhibit distinctive absorption peaks for Fe—O, hydroxyl, and silane functional groups. E) BET nitrogen adsorption–desorption isotherms displaying the surface area and porosity characteristics of magnetite, MMIP, and MNIP. F) Magnetization (M–H) curves showing the magnetic properties of magnetite and MMIP measured at room temperature.

C—C/C—H, and C═O bonds, respectively, indicating the presence of organic functional groups associated with the molecular imprinting process.[35] The N 1s spectrum (Figure S3C) displayed two peaks at 399.3 eV and 400.9 eV, which were assigned to the C—NH_2 and C—NH_3 groups, respectively, confirming the successful incorporation of amine functionalities from APTES.[36]

These XPS findings collectively validate the successful synthesis and surface modification of the MMIP and MNIP microparticles, demonstrating the effective coating of magnetite with a silane-functionalized polymeric shell. The presence of Si, N, C, and O functional groups endorses the formation of selective binding cavities, ensuring high specificity for ENF recognition and detection in electrochemical sensing applications.

2.1.3. FTIR Analysis

FTIR spectroscopic analysis was performed to further characterize the magnetite core and the MIP shell in the synthesized MMIP and MNIP microparticles. As shown in Figure 2D (black trace), the characteristic peaks at 595 and 488 cm^{-1} correspond to the Fe—O stretching vibrations, confirming the successful synthesis of magnetite NPs. The broad stretching vibration at 3440 cm^{-1}, along with the bending vibration at 1560 cm^{-1}, is attributed to the surface-adsorbed H_2O molecules, further validating the hydrophilic nature of the magnetite core.

Following surface functionalization and polymerization, distinct changes in the FTIR spectra were observed, confirming the formation of the molecularly imprinted polymer shell. As seen in the case of MMIP (red trace) and MNIP (blue trace), the characteristic peak at 1102 cm^{-1} corresponding to Si—O—Si asymmetric stretching, confirms the successful incorporation of TEOS during their polymeric shell formation. The additional peak at 1412 cm^{-1}, attributed to the symmetric stretching vibration of $–COO^-$ groups, suggests the presence of carboxylate moieties, likely originating from surface-functionalized magnetite NPs or residual polymerization precursors. Moreover, the peak at 1551 cm^{-1}, corresponding to N—H bending vibrations, reflects the contribution of APTES-derived amine functionalities within the polymeric framework. The absorption band at 1630 cm^{-1}, assigned to C═O stretching, further indicates the presence of carbonyl groups, which may result from the template imprinting or cross-linking process. Furthermore, a peak at 2933 cm^{-1}, corresponding to the C—H stretching vibrations of aliphatic $–CH_2$ and $–CH_3$ groups, is observed. This peak is primarily associated with the organic framework of the MIP and NIP, specifically arising from APTES and TEOS used in the polymerization process. The presence of this peak confirms the successful functionalization of the magnetite core with the imprinted polymer layer, as these aliphatic C—H bonds are characteristic of the silane coupling agents and polymeric network. These spectral features, along with Fe—O vibrations at 565 and 470 cm^{-1}, validate the core–shell

architecture of the MMIP, where magnetite serves as the magnetic core and the imprinted polymer provides selective binding sites for ENF. These findings corroborate the observations obtained from the XPS analysis and confirm the successful synthesis of MMIP particles with a well-defined magnetic core and a functionalized polymer shell.

2.1.4. BET Analysis

While polymerization and successful surface functionalization were confirmed through spectroscopic analysis, further investigation was required to understand how these modifications influenced the surface texture and porosity of the resulting materials. Therefore, nitrogen adsorption–desorption studies were conducted to evaluate the surface area, pore volume, and structural attributes of the MMIP and MNIP microparticles. The nitrogen adsorption–desorption isotherms of the MMIP and MNIP (Figure 2E) exhibit type IV behavior with H3 hysteresis, confirming the mesoporous nature (2–50 nm) of both materials, consistent with structures formed by particle aggregation.[37] The initial steep nitrogen uptake at low relative pressure ($P/P_0 < 0.05$) suggests the presence of micropores, while the increased adsorption at high P/P_0 (>0.8) indicates macropore filling. Notably, the MMIP demonstrates significantly higher nitrogen adsorption across all pressure ranges compared to the MNIP, implying an enhanced accessible pore volume resulting from the imprinting process. The BET analysis corroborates these findings, revealing a surface area of 23.78 $m^2\ g^{-1}$ for the MMIP, whereas the MNIP exhibits a significantly lower value of 13.34 $m^2\ g^{-1}$. This increased surface area enhances the accessibility of external binding sites and promotes faster mass transfer toward the imprinted cavities.

The BJH pore-size distribution (Figure 2E, inset) further elucidates these structural differences. The MMIP displays a well-defined pore-size distribution between 3.5–5 nm, corresponding to template-induced mesopores and interparticle voids. In contrast, the MNIP exhibits a peak near 3 nm with significantly reduced pore volume intensity, confirming the lack of template-directed porosity. These textural modifications account for the MMIP's superior adsorption performance. The extended mesoporous framework minimizes diffusion resistance while increasing the density of accessible recognition sites, leading to higher adsorption capacity and faster kinetics, as observed in subsequent studies. Such hierarchical pore structures and increased surface area not only contribute to efficient analyte binding but also enhance interfacial charge transfer, making MMIP an ideal candidate for electrochemical sensing applications. Thus, the imprinting process not only introduces molecular specificity but also refines the pore architecture, optimizing both adsorption capacity and sensing efficiency.

2.1.5. Magnetic Property Assessment

Following the textural analysis, magnetic characterization was performed to assess the impact of polymer encapsulation on the magnetic responsiveness of the synthesized materials. As magnetically assisted separation is integral part of the sensing platform's functionality, it was essential to ensure that the MMIP retained sufficient magnetic behavior post-polymerization, enabling efficient manipulation under an external magnetic field. For this, magnetic property assessments were done for the magnetite and MMIP particles to compare their magnetic characteristics at the pre- and post-fabrication stages. The magnetization versus magnetic field curve presented in Figure 2F illustrates the magnetic behavior of bare magnetite and MMIP particles under an applied field of + 16 000 to – 16 000 Oe at room temperature (300 K). The magnetite exhibits a higher saturation magnetization of 0.042 emu mg^{-1}, indicating strong magnetic properties, while MMIP shows a reduced saturation magnetization of 0.027 emu mg^{-1} due to the presence of the non-magnetic polymer shell. This decrease confirms the successful encapsulation of the magnetite core within the polymeric matrix, which is essential for selective molecular recognition. Despite this reduction, MMIP retains sufficient magnetic responsiveness for easy separation.[8] This also suggests that the polymer coating minimizes interparticle interactions and suppresses magnetic remanence, ensuring superparamagnetic-like behavior. The absence of significant hysteresis confirms that MMIP can be easily magnetized and demagnetized, which is crucial for reproducible magnetic separation in sensing applications.

2.2. Adsorption Study

Upon validating the structural, surface, and magnetic attributes of the synthesized MMIP and MNIP, we next investigated their functional performance through adsorption studies. These experiments were designed to examine the time-dependent uptake behavior and equilibrium binding capacity of MMIP and MNIP toward ENF, offering direct evidence of molecular recognition efficiency and the practical influence of the imprinting process.

2.2.1. Kinetic Adsorption Analysis

To understand the recognition behavior and extraction potential of MMIP and MNIP toward ENF, we have performed a series of adsorption studies. At first, time-dependent adsorption experiments were conducted using UV-vis spectroscopic analysis to investigate the adsorption kinetics of both polymers. As shown in **Figure 3A**, the MMIP exhibited a rapid adsorption phase within the first 5 min, achieving near-equilibrium at ≈35 min (t_e). This behavior is attributed to the abundance of specific binding cavities in the imprinted layer, enabling swift interactions with ENF. As these sites became progressively occupied, the adsorption rate declined and gradually reached a plateau. The adsorption capacity (Q_t) of MMIP was calculated using Equation (1).[38]

$$Q_t = \frac{(C_0 - C_t) \times V}{W} \quad (1)$$

where, Q_t is the adsorption capacity at time t (mg g^{-1}); C_0 and C_t are the concentrations of ENF (mg L^{-1}) at time 0 and t, respectively; V is the volume of the solution (L); and W is the mass of the adsorbent (g).

Q_t was found to be 250.04 mg g^{-1} at t_e. Whereas MNIP showed a much lower Q_t of 108.25 mg g^{-1}. The imprinting factor (IF),

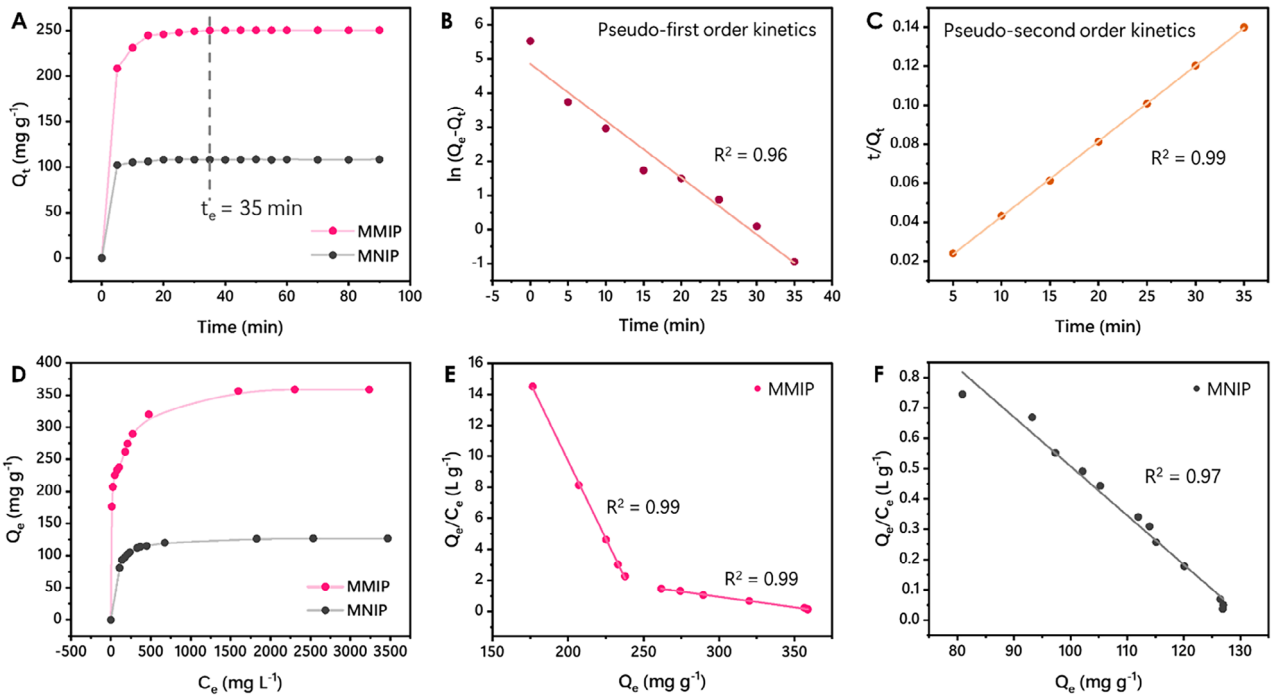

Figure 3. A) Time-dependent adsorption curves of ENF onto MMIP and MNIP showing rapid uptake and equilibrium behavior; B) pseudo-first-order kinetic fit for MMIP; C) pseudo-second-order kinetic fit for MMIP demonstrating superior correlation; D) adsorption isotherms of ENF onto MMIP and MNIP under optimized conditions; E) Scatchard plot of MMIP showing distinct high- and low-affinity binding regions; F) Scatchard plot of MNIP indicating a single, non-specific binding region. The results highlight the enhanced adsorption capacity, selectivity, and site heterogeneity introduced by molecular imprinting.

calculated as the ratio of MMIP to MNIP adsorption capacity ($Q_{t\text{-MMIP}}/Q_{t\text{-MNIP}}$), was 2.31, indicating a strong imprinting effect and high specificity of MMIP toward ENF. These results are summarized below in **Table 1**:

Table 1. Comparative adsorption performance of MMIP and MNIP microparticles toward ENF.

t_e [min]	Q_t-MMIP [mg g^{-1}]	Q_t-MNIP [mg g^{-1}]	$IF_{spectroscopic} = \frac{Qt-MMIP}{Qt-MNIP}$
35	250.041	108.245	2.31

To elucidate the adsorption mechanism, the kinetic data were fitted using the pseudo-first-order and pseudo-second-order models using Equations (2) and (3).[39]

$$\ln\left(Q_e - Q_t\right) = \ln Q_e - k_1 t \tag{2}$$

$$\frac{t}{Q_t} = \frac{1}{k_2 Q_e^2} + \frac{1}{Q_e} t \tag{3}$$

where Q_e is the adsorption capacity at equilibrium (mg g^{-1}), Q_t is the adsorption capacity (mg g^{-1}) at time t (min), k_1 is the pseudo-first-order adsorption rate constant (min^{-1}), and k_2 is the pseudo-second-order adsorption rate constant (g mg^{-1} min^{-1}).

As shown in Figure 3B,C, the pseudo-first-order model provided a reasonable fit ($R^2 = 0.96$); however, the pseudo-second-order model showed a superior correlation ($R^2 = 0.99$) value that closely matched the experimental result, supporting its validity. The stronger fit of the pseudo-second-order model is typically observed in MIPs due to their chemically selective recognition mechanisms. Unlike the pseudo-first-order model, which primarily describes physical adsorption governed by surface interactions, the pseudo-second-order model accounts for chemisorption, involving valence forces, electron sharing, or chemical bonding between the adsorbent and adsorbate.[40] In the context of MIPs, template molecules like ENF interact specifically with complementary functional groups embedded within the imprinted cavities, forming strong chemical interactions such as hydrogen bonding, electrostatic attractions, π–π stacking, or other non-covalent interactions.[41] As a result, MIPs commonly display adsorption kinetics that align more closely with pseudo-second-order models, as these models capture the chemical nature of binding and the gradual saturation of high-affinity sites. The kinetic fitting results obtained for MMIP are summarized below in **Table 2**.

Therefore, the excellent agreement with the pseudo-second-order kinetic model suggests that ENF adsorption onto MMIP is predominantly controlled by chemisorption through specific

Table 2. Kinetic modeling parameters for ENF adsorption onto MMIP.

Pseudo-first order kinetics		Pseudo-second order kinetics		
k_1 [min^{-1}]	R^2	Q_e [mg g^{-1}]	k_2 [g mg^{-1} min^{-1}]	R^2
0.167	0.96	258.4	0.00357	0.99

template–functional monomer interactions, underscoring the chemical selectivity inherent to molecularly imprinted polymers.

2.2.2. Adsorption Isotherm and Capacity

To systematically evaluate the adsorption characteristics of ENF onto the synthesized MMIP and MNIP, adsorption isotherm experiments were performed under optimized equilibrium conditions (35 min (t_e) incubation, pH 7.4). As illustrated in Figure 3D, the MMIP exhibited a pronounced increase in adsorption capacity with increasing initial ENF concentrations. Contrastingly, MNIP displayed a minimal and gradual rise in adsorption across the same concentration range. At the equilibrium concentration of adsorption (C_e), the adsorption capacity (Q_e) of the solution was determined using Equation (4).[42]

$$Q_e = \frac{(C_0 - C_e) \times V}{W} \tag{4}$$

where, Q_e is the adsorption capacity at equilibrium (mg g^{-1}); C_0 and C_e are the initial and equilibrium concentrations of ENF (mg L^{-1}), respectively; V is the volume of the ENF solution (L); and W is the mass of the adsorbent (g).

The calculated Q_e was found to be significantly higher (2.84 times) for MMIP (358.86 mg g^{-1}) compared to MNIP (126.43 mg g^{-1}). This observation highlights the enhanced affinity and selectivity demonstrated by the molecular imprinting process.

The observed maximum adsorption capacity of MMIP (358.86 mg g^{-1}) represents the real-world saturation limit attained under practical equilibrium conditions. Such elevated adsorption capacities in MIPs typically arise due to the presence of structurally tailored, selective binding cavities that form complementary interactions with the target molecule, ENF. These interactions include multiple specific binding mechanisms such as hydrogen bonding, stacking, electrostatic interactions, and hydrophobic forces. On the contrary, the much lower capacity observed in MNIP is attributable primarily to non-specific surface adsorption lacking any imprint-defined structural specificity.

To further characterize the binding specificity and heterogeneity of adsorption sites within MMIP, equilibrium adsorption data were analyzed using the Scatchard model (Equation 5).[43]

$$\frac{Q_e}{C_e} = \frac{Q_m}{K_d} - \frac{Q_e}{K_d} \tag{5}$$

where, Q_e equilibrium adsorption capacity of ENF at adsorption equilibrium (mg g^{-1}), C_e equilibrium concentration of ENF (mg L^{-1}), Q_m is the maximum theoretical adsorption capacity of the sorbent (mg g^{-1}), and K_d is the dissociation constant.

Figure 3E shows that the Scatchard plot of MMIP exhibited a clear deviation from linearity, resolved into two distinct linear segments, indicative of heterogeneous binding sites. Specifically, a high-affinity region with a low dissociation constant (K_d = 4.98 mg L^{-1}) and maximum binding capacity (Q_m) 248.40 mg g^{-1}, signifying the presence of highly selective, specifically imprinted binding sites with strong interactions toward ENF. The low-affinity region is characterized by a higher dissociation constant (K_d = 73.96 mg L^{-1}) and higher binding capacity (Q_m) = 369.91 mg g^{-1}, corresponding primarily to non-specific, weaker interactions involving surface-mediated binding. In contrast, the MNIP Scatchard plot (Figure 3F) exhibited a single linear region, indicating uniform binding sites with a moderate dissociation constant (K_d = 61.65 mg L^{-1}) and a low maximum binding capacity (Q_m = 131.25 mg g^{-1}). This homogeneous adsorption behavior corroborates the absence of structurally specific binding cavities, thus confirming non-selective and weak adsorption interactions. The detailed binding parameters derived from the Scatchard analysis for both MMIP and MNIP are summarized in **Table 3**, highlighting the distinct differences in affinity and capacity between the specific and non-specific binding sites.

Table 3. Binding parameters from Scatchard analysis highlighting site-specific interactions in MMIP and MNIP.

System	Binding Sites	K_d [mg L^{-1}]	Q_m [mg g^{-1}]	R^2	Binding impression
MMIP	High-affinity	4.98	248.40	0.99	Specific/imprinted sites
	Low-affinity	73.96	369.91	0.99	Non-specific binding
MNIP	Single-region	61.65	131.25	0.97	Lacks selective binding sites

It is important to note that the experimentally observed maximum adsorption capacity (Q_e = 358.86 mg g^{-1}) at equilibrium concentration (C_e) differs from the theoretically calculated Q_m value from the Scatchard model for the low-affinity region (369.91 mg g^{-1}). A similar observation was noted in the case of MNIP as well (Q_e = 126.43 mg g^{-1} and Q_m = 131.25 mg g^{-1} as observed maximum adsorption capacity and Q_m, respectively). Such differences are common in adsorption studies and arise because experimental conditions reflect practical equilibrium scenarios, while Scatchard analysis theoretically differentiates specific and non-specific binding sites through a mathematical interpretation of equilibrium data.[43] The experimentally measured adsorption capacity typically represents a realistic composite of both specific and non-specific interactions present simultaneously at equilibrium.

2.3. Binding Mechanism and Intermolecular-Force Analysis

The binding interactions between ENF and the MMIP were systematically investigated through FTIR spectroscopy, equilibrium binding studies, and kinetic analyses. As shown in Figure S4, notable spectral changes were observed when comparing the unloaded MMIP and the ENF-loaded MMIP. Specifically, the C=O stretching band at 1630 cm^{-1} exhibited a distinct downshift to 1625 cm^{-1} upon ENF binding, indicative of possible hydrogen bonding interactions between the carbonyl functionalities of ENF and the complementary groups within the polymeric matrix. Additionally, the N–H bending vibration previously at 1551 cm^{-1} became broader and slightly upshifted to 1560 cm^{-1}, further supporting the involvement of amine groups in hydrogen bond formation. These findings are consistent with previously reported literature.[44] A prominent increase in the intensity of the absorption band around 1385–1390 cm^{-1}, corresponding to the symmetric stretching of carboxylate ($–COO^-$) groups, was also

observed. This feature is consistent with the establishment of electrostatic interactions between the carboxylate moieties of ENF and the protonated amine ($-NH_3^+$) groups present in the polymer. These interaction-specific spectral changes were absent in the MNIP control, thereby highlighting the imprinting-driven selective recognition of ENF by the MMIP system.

The binding behavior was further elucidated through Scatchard analysis, which revealed two distinct binding populations in the MMIP (Figure 3E). The high-affinity sites had a dissociation constant ($K_{d\text{-}High}$) of 4.98 mg L^{-1} and a maximum adsorption capacity (Q_{mH}) of 248 mg g^{-1}. The low-affinity sites showed $K_{d\text{-}Low}$ = 73.96 mg L^{-1} and Q_{mL} = 370 mg g^{-1}. In contrast, the MNIP displayed only a single, weaker binding site population with K_d = 61.65 mg L^{-1}. After conversion to molar units, the $K_{d\text{-}High}$ was 1.38 × 10^{-5} M, and the $K_{d\text{-}Low}$ was 2.06 × 10^{-4} M. The standard Gibbs free energy (ΔG°), calculated using Equation 6.[45]

$$\Delta G^\circ = -RT \ln K_\alpha = RT \ln K_d \quad (6)$$

where ΔG° represents standard Gibbs free energy change of binding (J mol^{-1}), R denotes universal gas constant (8.314 J mol^{-1} K^{-1}), T denotes absolute temperature (298 K), K_a denotes association constant of the binding interaction (L mol^{-1}), K_d denotes dissociation constant of the binding interaction (mol L^{-1}), where $K_\alpha = 1/K_d$.

The evaluated ΔG° was found to be –27.7 kJ mol^{-1} for the high-affinity sites and –21.0 kJ mol^{-1} for the low-affinity sites. These values suggest that the high-affinity sites are driven by strong hydrogen bonding and electrostatic interactions, while the low-affinity sites rely mainly on weaker nonspecific forces, such as hydrophobic and van der Waals interactions.

Kinetic analyses further supported these observations (Figure 3B,C). ENF adsorption onto the MMIP followed a pseudo-second-order kinetic model, with an excellent fit (R^2 = 0.99), suggesting that chemisorption, involving valence-type forces, controls the uptake process. Notably, the initial adsorption rate for the MMIP was substantially higher than that of the MNIP, underscoring the critical role of imprinting in enhancing both binding strength and adsorption kinetics. The binding mechanism can be described as a cooperative process, where ENF initially interacts with the imprint cavity through hydrophobic and π–π interactions. This is followed by the formation of strong hydrogen bonds and an electrostatic clamp between the ENF carboxylate and the polymer's protonated amine groups. Collectively, these factors explain the superior adsorption performance and sensing capability of the MMIP system.

2.4. Electrochemical Characterization of Modified Electrode Surface

While the adsorption studies established the selective recognition and binding efficiency of MMIP toward ENF under equilibrium and kinetic conditions, these findings needed to be validated under electrochemical settings to demonstrate practical sensing applicability. Therefore, the stepwise fabrication of the sensing probe was electrochemically characterized to evaluate charge transfer behavior, interfacial resistance, and the functional contribution of each modification layer, ultimately confirming the integration and performance of the MMIP-based electrochemical sensor. The stepwise fabrication of the ENF sensing probe, as shown in Scheme 2B was electrochemically characterized using CV and EIS to assess its charge transfer behavior and stability (**Figure 4**). For this purpose, 0.5 mM Zobell's solution (ZS) was employed as a redox probe to evaluate the electrochemical responses at each modification step.

First, to confirm the successful electrodeposition of AuNPs onto the WE, LSV was performed over three consecutive scans. A distinct reduction peak at +0.92 V (versus Ag/AgCl) was observed, corresponding to the electrochemical reduction of gold ions, a phenomenon associated with the stripping of deposited AuNPs. This observation, consistent with our previous study, confirms the formation of a conductive gold layer that enhances the electrode's charge transfer properties.[46] The increase in current peak intensity (Figure S5) with subsequent scans further indicates the progressive growth of AuNPs, leading to improved surface conductivity and electron transfer efficiency. Following AuNP deposition, the electrode (AuNP/WE) was modified with reduced graphene oxide (rGO) to form the rGO/AuNP/WE probe, which further enhances electron transfer kinetics. The CV responses were recorded for the step-by-step fabrication of AuNP/WE and then rGO/AuNP/WE electrodes. A potential window of −0.6 to +0.9 V (versus Ag/AgCl) and a scan rate of 50 mV s^{-1} was used as optimized analytical parameters. Figure 4A,B shows the representative voltammograms for the redox process of $[Fe(CN)_6]^{3-/4-}$ at the bare WE (red trace), AuNP/WE (orange trace), and rGO/AuNP/WE (green trace). Notably, the AuNP/WE electrode exhibited enhanced anodic (I_{pa}) and cathodic (I_{pc}) peak currents, attributed to the deposition of AuNPs on the WE surface, which increases conductivity and effective surface area for charge transfer. Similarly, the rGO/AuNP/WE probe demonstrated a further increase in both I_{pa} and I_{pc}, owing to the high conductivity and large surface area of rGO. However, upon subsequent deposition of the MMIP microparticles, a significant decrease in redox peak current was observed for the final sensing probe, MMIP/rGO/AuNP/WE (purple trace). This attenuation can be attributed to the diffusion-limiting effect of the organic polymer shell, which introduces a physical barrier to electron transfer, thereby increasing the resultant surface resistance. It should be noted that AuNPs and rGO were used to improve the total conductivity and support smooth electron transfer and to reduce the resistance caused by the MMIP layer on the final sensing probe.

To complement the CV findings and further analyze the charge transfer behavior, EIS was performed, and the spectral data were represented using a Nyquist plot (Figure 4C). The inset of Figure 4C represents Randle's circuit used to interpret the charge transfer resistance (R_{ct}) (Figure 4D) and the overall electrochemical behavior of the fabrication stages of the final sensing probe (MMIP/rGO/AuNP/WE). The bare WE exhibited a high R_{ct} of 756.41 ± 13.04 Ω, indicating limited electron mobility (red curve). Upon AuNP deposition, the R_{ct} significantly decreased to 311.12 ± 11.77 Ω, due to the excellent conductivity and catalytic properties of AuNPs (peach curve). A further reduction in R_{ct} to 262.74 ± 8.56 Ω was observed upon rGO functionalization,

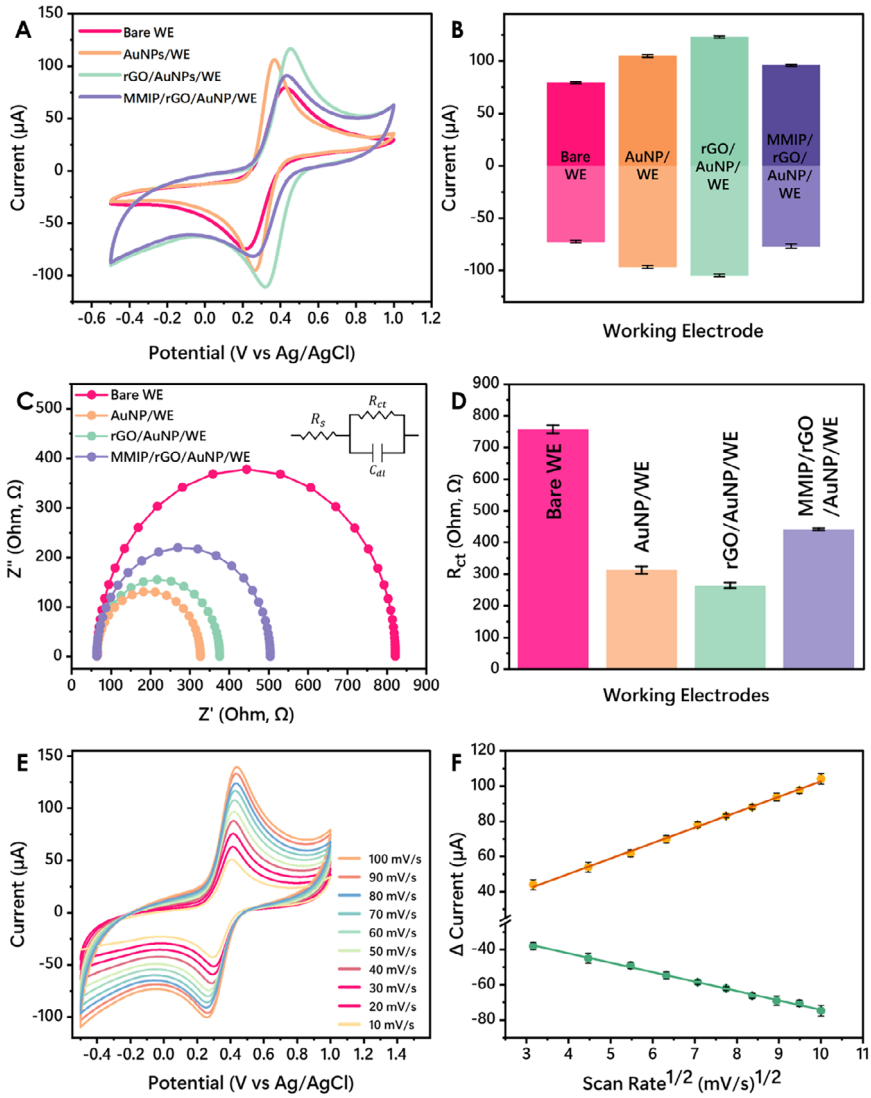

Figure 4. Electrochemical characterization of the sensor probes. A) CV of bare WE working electrode (pink trace), AuNP/WE (orange trace), rGO/AuNPs/WE (green trace), MMIP/rGO/AuNPs/WE (blue trace). B) Comparative histogram of respective electrode surfaces; C) EIS response of CV of bare WE working electrode, AuNP/WE, rGO/AuNP/WE, MMIP/rGO/AuNP/WE. D) Shows the comparative histogram of the derived R_{ct} values from the respective electrode surfaces; E) scan rate study of final MMIP/rGO/AuNP/WE modified surface from 10 to 100mV s^{-1} and showed that as scan rate increases the current response also increases due incremental availability of ENF at the electrode surface; F) Linear fitting of corresponding scan rate.

confirming its role in facilitating charge transfer (green curve). However, immobilizing MMIP on the sensing probe increased the R_{ct} to 440.40 ± 3.83 Ω, consistent with the insulating nature of the polymer shell, which restricts electron flow and confirms the successful formation of the imprinted polymeric interface. The variations in R_{ct} values at each step provide clear electrochemical evidence of progressive sensor fabrication, corroborating the CV findings.

Since the performance of such probes depends on their stability and electrochemical kinetics, a control experiment was conducted to assess the stability of the sensor system. For this, a scan rate study was performed using CV at various scan rates ranging from 10 to 100 mV/s (Figure 4E). The results showed that both I_{pc} and I_{pa} were directly proportional to the square root of the scan rate (Figure 4F), yielding correlation coefficients of 0.99, indicative of a diffusion-controlled charge transfer process. This finding confirms the stable and reproducible nature of the sensor, reinforcing its suitability for real-time electrochemical ENF detection.

The integration of MMIPs with magnetic properties in the sensor design provides additional advantages by enabling efficient separation of ENF from complex sample matrices. The combination of AuNPs, rGO, and molecular imprinting technology enhances the sensor's selectivity, sensitivity, and stability, making it a promising platform for high-performance electrochemical sensing applications. These findings establish the MMIP-based sensor probe as an effective tool for on-site antibiotic residue detection, with potential applications in food safety

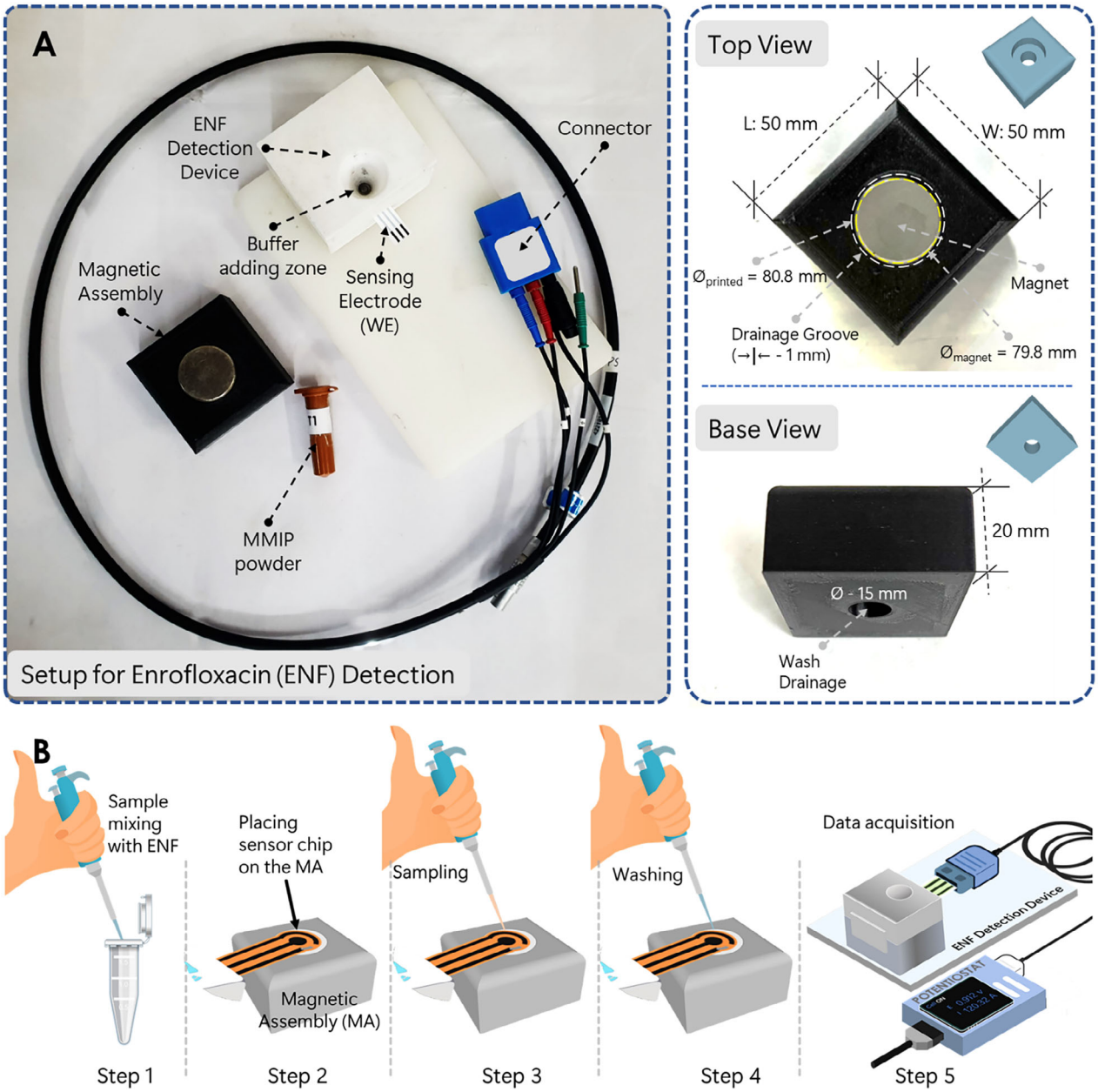

Figure 5. A) Prototype device setup for electrochemical detection of ENF. (Left) Real image of the developed device, including the magnetic assembly, ENF detection unit, MMIP powder, fabricated sensor chip, and connector for potentiostat integration. (Bottom Right) Dimensional schematic of the 3D-printed magnetic assembly, designed for efficient MMIP separation and sensor operation. B) Schematic representation of the five-step process for ENF detection: (1) Mixing of buffer sample with MMIP powder, (2) Magnetic separation of ENF-bound MMIPs, (3) Loading of MMIP microparticles onto the sensor chip, (4) Washing to remove unbound ENF molecules, and (5) Electrochemical measurement using the potentiostat system.

monitoring, environmental surveillance, and pharmaceutical quality control.

2.5. Miniaturized Device Prototyping for the Electrochemical Detection of ENF

For enhanced practicality and ease of application, we have developed a device prototype for the electrochemical detection of ENF (**Figure 5**). The device integrates an MMIP-based sensing approach with a custom-designed electrochemical sensor chip. Figure 5A illustrates the complete setup, which comprises a magnetic assembly for MMIP separation, synthesized MMIP powder for selective ENF encapsulation, a fabricated ENF sensor chip, an ENF detection device housing the sensor chip and sample, and a connector unit that interfaces the sensor with the potentiostat system for electrochemical measurements.

A critical component of the setup is the 3D-printed magnetic assembly, designed for efficient magnetic separation of MMIPs. The top view reveals a compact structure measuring 50 mm × 50 mm, with a circular cavity of 80.8 mm diameter ($ø_{printed}$) that securely holds a 79.8 mm diameter ($ø_{magnet}$) magnet. A precisely designed 1 mm thick drainage groove facilitates controlled liquid handling during sample preparation, while the base view displays a 15 mm drainage outlet that effectively removes unwanted components, ensuring a clean sensing environment. The ENF detection follows a systematic five-step process depicted in Figure 5B. Step 1 involves mixing 1 mL of buffer sample with 1 mg of MMIP powder in a sample tube and incubation. In Step 2, the fabricated sensor chip (rGO/AuNP/WE) is placed over the magnetic assembly to initiate the magnetic separation of ENF-bound MMIPs. Step 3 involves loading these MMIP microparticles onto the sensor chip. Step 4 introduces a washing step to remove unbound ENF molecules, ensuring only ENF bound to the magnetically active MMIPs remains on the sensor surface. The **Supplementary Video File** highlights the advantage of using magnetic MIP particles for rapid separation under an external magnetic field. In the final step (Step 5), the functionalized sensing probe (MMIP/rGO/AuNP/WE) is integrated into the ENF detection device. A buffer is added to the designated zone, and the probe is connected to the potentiostat system for electrochemical measurements. This integrated approach combines molecular imprinting with electrochemical sensing, ensuring high selectivity and sensitivity for ENF detection. The strategic use of MMIPs enables targeted analyte capture, while the custom-designed magnetic assembly streamlines sample processing, making the system a robust platform for monitoring antibiotic residues in dairy products.

2.6. Analytical Performance of the Final Sensing Sensor Probe

The developed sensor probe underwent extensive physical and electrochemical characterization to validate its structural and functional attributes (**Figure 6**). Electrochemical assessments were conducted using the prototyped device, following the prescribed 5-step process. DPV was employed to evaluate the sensor's response to ENF, with phosphate-buffered saline (PBS, pH 7.0) serving as the buffer electrolyte. To establish baseline performance, the final sensor probe (MMIP/rGO/AuNP/WE) was first analyzed in PBS without ENF as a negative control, confirming no current due to the absence of electron transfer between the electrode and analyte (Figure 6A, purple trace). This observation also ensures no significant background current contribution to the system.

Upon assessing the AuNP/WE (orange trace) and rGO/AuNP/WE with ENF [10^{-6} M] (yellow trace), a minor but insignificant response peak near +0.8 V (vs Ag/AgCl) was noticed, which has been reported as the fingerprint oxidation potential region for ENF.[47] This weak signal likely resulted from residual unadsorbed ENF and reinforces the importance of MMIP microparticles for selective analyte capture. The pink trace (WE with ENF [10^{-6} M]) further confirms that, in the absence of AuNPs, rGO, and MMIP, the sensor fails to facilitate significant electron transfer, exhibiting the lowest signal generation. In contrast, the blue trace, corresponding to MMIP/rGO/AuNP/WE in the presence of ENF [10^{-6} M], displays a distinct and prominent oxidation peak near +0.8 V (versus Ag/AgCl), affirming selective ENF binding via artificial recognition cavities and enhanced electron transfer facilitated by the AuNPs and rGO nanocomposite. This highlights the key role of the MMIP layer in providing specific and high-affinity recognition of ENF. To further assess the influence of non-imprinted controls, the sensor probe modified with MNIP (MNIP/rGO/AuNP/WE) microparticles was evaluated (green trace). Here, a minor oxidation peak was observed, which is consistent with nonspecific adsorption of ENF onto the polymeric surface of the MNIP particles. As supported by the adsorption isotherm data, the MNIP exhibited a single, low-affinity binding region, reflecting nonselective surface interactions rather than specific cavity-driven recognition. These weak, nonspecific interactions allow limited ENF accumulation at the sensor surface, leading to a small but detectable electrochemical response. Importantly, the magnitude of this response remains significantly lower compared to the MMIP-based sensor, underscoring the critical role of molecular imprinting in enhancing selective binding and signal amplification. Figure 6B presents the quantitatively compared histogram, corresponding to the change in current (Δ Current) across different electrode configurations. The MMIP/rGO/AuNP/WE sensor probe exhibits the highest Δ Current in the presence of ENF [10^{-6} M], due to the synergistic effects of selective ENF binding and enhanced charge transfer kinetics facilitated by the nanocomposite-modified surface. The probable electrooxidation reaction of ENF on the fabricated electrode surfaces is shown in Figure 6C, as also proposed in the previous literatures.[48,49]

The device's performance was further evaluated across a wide range of ENF concentrations (10^{-10} to 10^{-2} M), as depicted in Figure 6D. The DPV responses exhibit a systematic increase in oxidation peak current near +0.8 V (versus Ag/AgCl) with increasing ENF concentration, validating the device's dynamic response. The corresponding calibration plot (Figure 6E) demonstrates a linear detection range (LDR) spanning 10^{-10} to 10^{-2} M, with a regression equation: ΔI (Δ Current) = 81.84 (±0.75) + 6.54 (± 0.11) × Log Conc. [ENF (M)].

A high correlation coefficient (R^2 = 0.98) confirms excellent linearity. The limit of detection (LOD) was determined using Equation (7), which was found to be 1.61 (± 0.02) × 10^{-13} M (161 fM) (RSD < 2.15%, n = 3, 95% confidence interval), highlighting the device's ultrasensitive detection capability.

$$Limit\ of\ Detection = \frac{3\sigma_b}{m} \tag{7}$$

where σ_b is the standard deviation of the blank and m is the slope of the calibration curve.

To further evaluate the imprinting effect, calibration was also performed using the MNIP-based probe under identical conditions across the same ENF concentration range (10^{-10} to 10^{-2} M) (Figure S6). Based on the regression equation derived from the calibration plot (Figure 6E), the MNIP sensor displayed weak, nonspecific interactions and poor analyte accumulation on the non-imprinted surface. The regression equation for the MNIP calibration was determined to be: ΔI = 6.78 (±0.46) + 0.46 (± 0.06) × Log Conc. [ENF (M)] with a correlation coefficient (R^2) of 0.94.

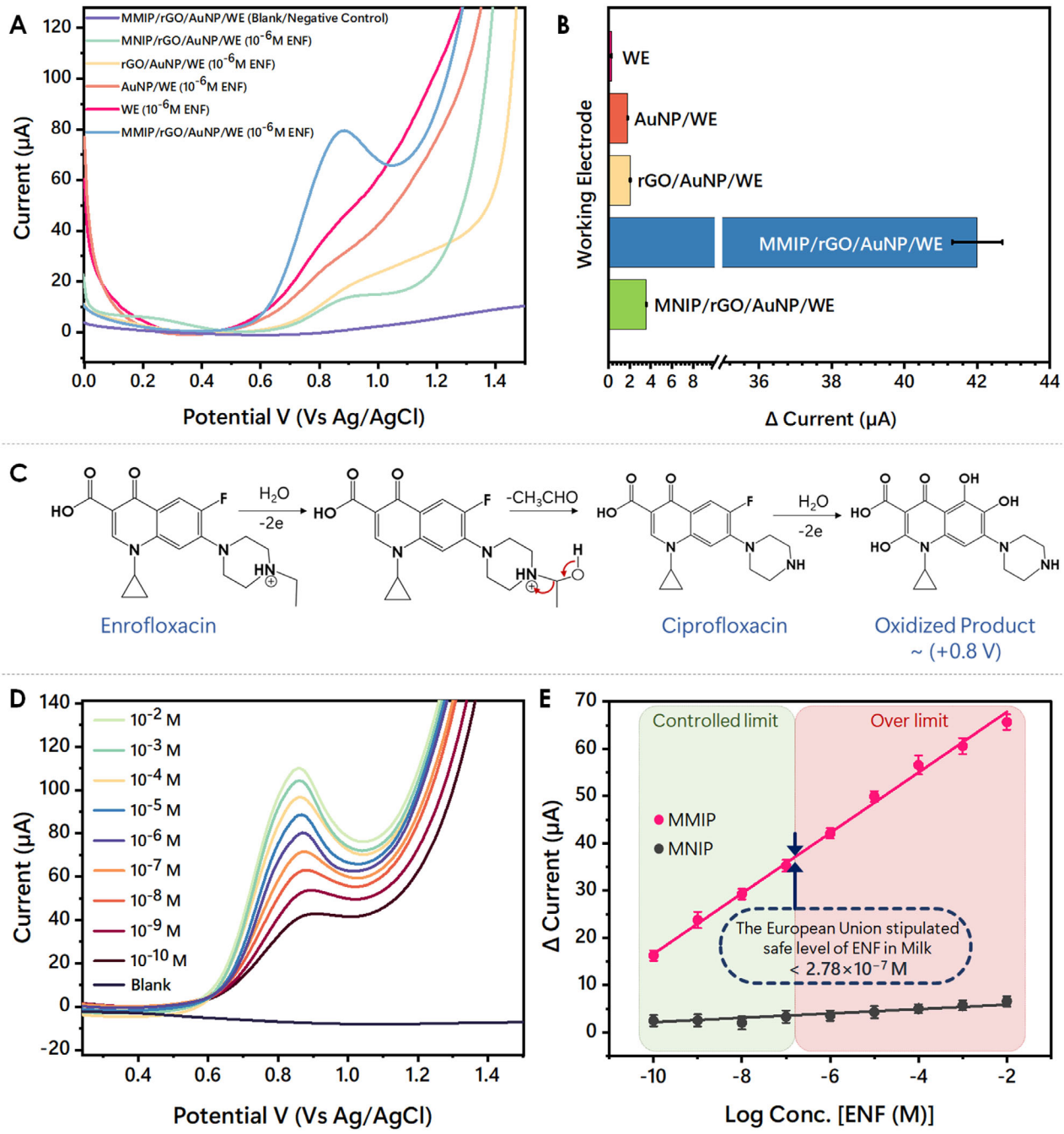

Figure 6. A) Comparative DPV responses of the stepwise fabrication of the MMIP/rGO/AuNP/WE probe and its analytical significance. B)Corresponding histograms of the peak currents obtained from the voltammetric responses, highlighting the enhanced signal for the MMIP/rGO/AuNP/WE probe. C) Schematic representation of the probable ENF electrooxidation on the fabricated electrode, highlighting the chemical transformation and electron transfer process. D) DPV responses of the MMIP/rGO/AuNP/WE probe for varying ENF concentrations (10^{-10} to 10^{-2} M), demonstrating the sensor's dynamic range. E) Calibration plot corresponding to the voltammetric responses for MMIP (red) and MNIP (black) in response to ENF concentrations (10^{-10} to 10^{-2} M).

Further, the IF was recalculated using Equation (8), based on the slope values obtained from the respective calibration equations.[50] Importantly, the IF provides a quantitative measure of imprinting efficiency by comparing the binding or response of the imprinted and non-imprinted systems. A higher IF value directly reflects superior selectivity, recognition ability, and binding affinity of the MMIP toward the target analyte.

$$IF_{Electrochemical} = \frac{\text{Slope}_{MMIP}}{\text{Slope}_{MNIP}} \quad (8)$$

The derived IF value was found to be 14.15 for the synthesized MMIP. Interestingly, this IF is much higher than the IF obtained from the adsorption isotherm data. This enhancement may be attributed to the broader dynamic detection range and superior signal amplification provided by the electrochemical platform, which is inherently limited in conventional UV-vis-based equilibrium measurements. Notably, the integration of AuNPs and reduced graphene oxide (rGO) onto the electrode surface significantly contributed to this performance boost by enhancing electron transfer kinetics, increasing electroactive surface area, and improving signal-to-noise ratio. Together with the selective binding capability of MMIP, this nanocomposite-engineered interface enabled more sensitive and selective detection of ENF, underscoring the synergistic advantage of molecular imprinting and nanomaterial-assisted electrochemical transduction. It is worth mentioning that the sensor's dynamic range supports the Maximum Residual Limits (MRLs) for ENF in food items, which have been regulated at 2.78×10^{-7} M by the European Commission. These findings establish the MMIP/rGO/AuNP/WE sensor probe as a highly selective and sensitive platform for ENF detection in laboratory or industrial settings.

After evaluating the analytical performance of our developed sensor platform for ENF detection, we conducted a detailed comparative analysis with previously reported electrochemical sensors, as summarized in **Table 4**. The comparison includes key physical and analytical parameters such as fabrication methods, detection ranges, LOD, and applicability to real samples, providing a comprehensive assessment of their relative performance compared to our system.

2.7. Sensitivity and Selectivity Assay

The sensitivity of a sensor is a critical parameter that defines its ability to detect low concentrations of the target analyte at ambient conditions.[28] In this study, the sensitivity of the developed electrochemical sensor was evaluated by calculating the active surface area (A) of the electrode and determining the sensitivity coefficient. The active surface area was calculated using the Randles-Sevcik equation (Equation 9):

$$I_p = \left(2.69 \times 10^5\right) \cdot n^{3/2} \cdot A \cdot D^{1/2} \cdot C \cdot \nu^{1/2} \quad (9)$$

where **Ip** is peak current (A), **n** is number of electrons transferred in the redox reaction (here, n = 1), **A** is active surface area (cm^2), **D** is diffusion coefficient of the redox probe ($D = 7.6 \times 10^{-6}$ cm^2 s^{-1}), **C** is concentration of the redox probe ($C = 5 \times 10^{-6}$ mol cm^{-3}), ν is the scan rate ($\nu = 0.05$ V s^{-1}).

Using the measured peak current ($Ip = 72.86 \times 10^{-6}$ A), the active surface area was calculated to be **0.79 cm^2**. The sensitivity coefficient was then determined as the ratio of the slope value (m = 6.54 µA per decade) of the calibration curve and the calculated active surface area:

$$Sensitivity = \frac{m}{A} = \frac{6.54\mu A/decade}{0.79\ cm^2} = 8.28\mu A/decade/cm^2 \quad (10)$$

This high sensitivity ensures that the sensor can accurately detect ENF even at low concentrations, making it suitable for trace-level analysis.

The selectivity of the sensor is equally important, as it ensures that the sensor responds specifically to the target analyte (ENF) without interference from other molecules. To evaluate selectivity, the sensor's responses were tested in the presence of various potential interfering molecules commonly found in milk samples, which we have considered as the real sample matrix (**Figure 7A**). The interfering molecules included glucose, lactose, ascorbic acid, urea, casein, L-histidine, L-methionine, thiamine (Vitamin B1), and niacinamide (Vitamin B3). Each interfering molecule was tested at a concentration higher than its typical level in biological samples to assess its potential impact on ENF detection.

As shown in Figure S7, the comparative histogram illustrates that these interfering molecules exhibited negligible (<0.27%) or no deviation in the oxidation current compared to ENF (10^{-6} M). This indicates that the interfering species are either electrochemically inactive within the selected potential window or possess different redox potentials, preventing interference with ENF detection. The selectivity coefficient (K_{sel}) of the final probe is determined by Equation (11).

$$K_{Sel.} = \frac{\left[Signal\right]_{Interfering\ molecules}}{\left[Signal\right]_{ENF}} \quad (11)$$

[Signal]$_{\text{Interfering molecules}}$ denote the corresponding current signals that refer to molecules that disrupt or affect the signal strength exhibited by a probe when it is exposed to them, and **[Signal]$_{\text{ENF}}$** denotes the signal strength corresponding to ENF.

The calculated K_{sel} values for all the interfering molecules were found to be significantly low ($K_{sel} \ll 1$), confirming the sensor's high selectivity toward ENF. To further validate these results, a T-test was conducted, and the p-values for ENF against all interfering molecules were found to be < 0.001 (n = 5), indicating statistically significant differences. The high sensitivity of the sensor, as also demonstrated by the low detection limit and large active surface area, ensures accurate detection of ENF even at trace levels. Simultaneously, the excellent selectivity ensures that the sensor's response is specific to ENF, even in the presence of potentially interfering molecules commonly found in complex matrices like milk. This combination of high sensitivity and selectivity makes the developed sensor a reliable and robust platform for real-sample analysis.

To further investigate the molecular imprinting-derived specificity of the developed MMIP sensor, selectivity experiments were conducted using structurally related fluoroquinolone antibiotics, namely CIP, NOR, and OFL. These analogs were tested at a concentration of 1 µM (10^{-6} M), following the same incubation and measurement protocol as used for ENF. The DPV responses were carefully recorded, focusing on the Δ Current values specifically at the characteristic oxidation potential of ENF (≈ +0.8 V versus Ag/AgCl), ensuring an accurate and comparable assessment across all analytes (Figure 7B). The MMIP-modified sensor exhibited a pronounced current response for ENF, with a Δ Current of 41.59 (±3.19) µA, consistent with the high-affinity, selective binding expected from the imprinting process. In contrast, the responses for CIP, NOR, and OFL were substantially lower registering Δ Current values of 7.92 µA (±1.22), 5.12 µA (±0.88), and 3.93 µA (±0.90), respectively. The significantly reduced

Table 4. Comparison of the developed MMIP-based electrochemical sensor with previously reported sensors for ENF detection, highlighting electrode modifications, detection range, LOD, and real sample applicability.

S. No.	Modified electrode	Fabrication strategies	Technique	Linear range [M]	LOD (M)	Real sample	Ref.
1	TAPB-PDA-COFs/AuNPs/GCE	The glassy carbon electrode was modified with gold nanoparticles, covalent organic framework, p-phthaldehyde, and then tris aminophenyl benzene to obtain the final sensor probe	SWV	$5.0 \times 10^{-8} - 1.2 \times 10^{-4}$	4.1×10^{-8}	Yes	[21]
2	APT-BDD	Boron-doped diamond electrode was pretreated anodically to obtain APT-BDD	DPV	$7.0 \times 10^{-8} \cdot 2.8 \times 10^{-6}$	1.6×10^{-8}	Yes	[51]
3	Bare GCE	A pretreated glassy carbon electrode was used to detect enrofloxacin in diverse matrices	SWV	$1.0 \times 10^{-6} - 3.0 \times 10^{-5}$	$1.64 (\pm 0.3) \times 10^{-6}$	Yes	[52]
4	MIP/PGE	Molecularly imprinted polymer was directly electropolymerized onto the pencil graphite electrode	SWV	$1.0 \times 10^{-10} - 1.0 \times 10^{-4}$	6.57×10^{-13}	Yes	[53]
5	Fe_3O_4/MWCNT/CPE	Carbon paste electrode (CPE) was modified with multiwalled carbon nanotube and Fe_3O_4 nanoparticle	DPV	$3.0 \times 10^{-7} - 1.0 \times 10^{-4}$	9.0×10^{-8}	Yes	[54]
6	MWCNT/GCE	The glassy carbon electrode was modified with multiwalled carbon nanotube	LS-SVM LSV	$2.0 \times 10^{-6} - 7.8 \times 10^{-4}$ $3.0 \times 10^{-6} - 1.2 \times 10^{-3}$	5.0×10^{-7} 9.0×10^{-7}	Yes	[55]
7	CdS@ENR-TPB	Cadmium solution was dispersed with ethanol and doped into the ethanolic solution of ENF to obtain CdS@ENR-TPB	CV	$1.0 \times 10^{-7} - 1.0 \times 10^{-2}$	9.5×10^{-8}	Yes	[22]
8	CW/RGO/RRDE	The rotating ring disk electrode (RRDE) was modified with reduced graphene oxide and calcium tungstate	AMP	$1.0 \times 10^{-9} - 1.15 \times 10^{-4}$	2.1×10^{-8}	Yes	[49]
9	MMIP/rGO/AuNP/WE	Stepwise electrode modification with AuNPs, rGO, and MMIP on a working electrode (WE), integrated into a 3D-printed magnetic-assisted sensing device	DPV	$1.0 \times 10^{-10} - 1.0 \times 10^{-2}$	$1.61 (\pm 0.02) \times 10^{-13}$	Yes	This Work

Abbreviation- SWV: Square Wave Voltammetry, DPV: Differential Pulse Voltammetry, LS-SVM: Least Squares Support Vector Machine, LSV: Linear Sweep Voltammetry, CV: Cyclic Voltammetry, AMP: Amperometry

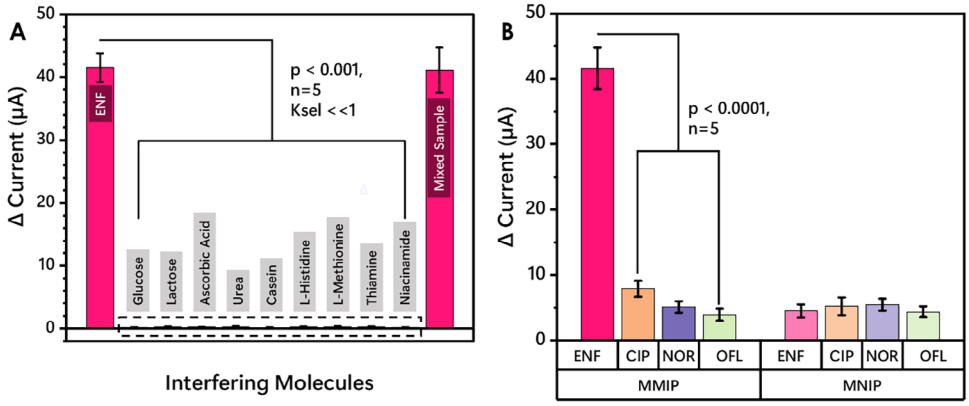

Figure 7. Selectivity assessment of the MMIP-based sensor for ENF detection. A) DPV responses in the presence of potential interfering molecules commonly found in milk. B) Selective response of the MMIP and MNIP sensor toward ENF compared to structurally similar fluoroquinolone antibiotics (ciprofloxacin, norfloxacin, and ofloxacin), demonstrating the imprinting effect.

Δ currents observed for the analogs can be attributed not only to their differing redox potentials[56–58] but also to their partial structural resemblance to ENF, which permits limited nonspecific interactions with the imprinted cavities. These interactions likely arise from common fluoroquinolone features such as the piperazine ring and quinolone backbone, which can weakly interact via hydrogen bonding or π–π stacking with the polymer matrix. However, due to the absence of the precise size, shape, and functional group complementarity imprinted for ENF, these analogs fail to achieve high-affinity binding, leading to markedly attenuated signals.

Interestingly, the MNIP-modified control sensor exhibited uniformly low and nonspecific responses across all tested compounds: Δcurrent for ENF was 4.51 μA (±0.98), for CIP 5.24 μA (±1.37), for NOR 5.48 μA (±0.92), and for OFL 4.39 μA (±0.80). This indicates that, in the absence of molecular imprinting, the system primarily relies on weak surface adsorption and electrostatic interactions, lacking the selective recognition capability required for discriminating ENF from its analogs. The slightly higher responses observed for CIP and NOR on the MNIP may result from their relatively stronger nonspecific adsorption on the polymer surface, likely influenced by differences in their diffusion coefficients, redox activities, or surface affinities compared to ENF and OFL. The comparative analysis of Δcurrent values underscores the exceptional selectivity of the MMIP system toward ENF, with a signal enhancement of approximately 5.25-fold over CIP, 8.12-fold over NOR, and 10.58-fold over OFL. This selectivity is primarily governed by the synergistic effects of molecular imprinting and nanomaterial-enhanced electrochemical transduction, which together ensure that only the target molecule, ENF, achieves efficient preconcentration and electron transfer at the electrode surface. Importantly, the oxidation signals recorded for each analyte were confirmed to originate specifically from the ENF oxidation potential region, eliminating the possibility of overlapping redox processes or matrix-related interferences. These findings highlight the robust molecular recognition capability of the MMIP-based sensor and its promising application for selective ENF detection in complex sample matrices.

2.8. Real Sample Analysis

To evaluate the practical applicability of the developed electrochemical sensing device, real sample analysis was conducted using commercially available milk samples purchased from a local grocery store. A standard addition mathematical model was employed to determine the sensor's effectiveness in detecting ENF. Known concentrations of ENF ranging from 10^{-8} to 10^{-4} M were spiked into the milk samples, and the DPV responses from the sensing device were recorded and compared to the standard buffer solutions. The percentage recovery was calculated using Equation (12), which quantifies the accuracy of the device's detection capability in real samples.

$$\%\text{Recovery} = \frac{[S]_{ENF} - [B]_{ENF}}{[SS]_{ENF}} \quad (12)$$

where, $[S]_{ENF}$ and $[B]_{ENF}$ are the analytical responses of ENF in the spiked and blank milk samples, respectively; and $[SS]_{ENF}$ is the analytical response of ENF in the standard buffer solutions.

The results, presented in **Table 5**, demonstrate high recovery rates ranging from 90.23% to 97.29%, confirming the device's reliability in detecting ENF in milk. The ENF detection procedure follows the same prescribed steps (Figure S8) to ensure effective extraction and quantification. Initially, 1 mL of raw milk is mixed with 1 mg of MMIP powder in the sampling tube, enabling selective binding of ENF through MMIP interactions. The bound ENF-MMIP complex is then isolated using a magnetic separation technique, which eliminates unbound components and enhances sample purity. The ENF-loaded MMIPs are subsequently transferred onto the fabricated electrochemical sensor chip for further analysis. To minimize matrix interference, a washing step is performed to remove non-specifically bound molecules. Finally, electrochemical measurements are conducted using a potentiostat system, ensuring precise and selective detection of ENF.

The integration of molecular imprinting technology with electrochemical sensing provides a highly specific and sensitive approach to antibiotic residue detection in dairy products. The

Table 5. Real sample analysis of ENF detection using the developed MMIP-based electrochemical sensor, representing the spiked ENF concentrations, corresponding voltammetric responses, and the obtained ENF responses.

Spiked ENF concentration [M]	Current responses in Buffer (Standard) ΔI [μA]	Obtained ENF responses in the Milk Sample		
		ΔI [μA]	% RSD [n = 3]	% Recovery
1×10^{-4}	56.59 (±1.09)	55.05 (±1.11)	3.47	97.29
1×10^{-5}	49.92 (±1.27)	46.65 (±0.91)	3.39	93.44
1×10^{-6}	42.12 (±1.09)	38.38 (±1.01)	4.43	90.56
1×10^{-7}	35.29 (±1.32)	31.83 (±0.82)	4.69	90.23
1×10^{-8}	29.27 (±1.15)	26.67 (±0.32)	2.12	91.15

incorporation of 3D-printed magnetic assemblies streamlines sample preparation, improving processing efficiency. As evident from Table 5, the current responses from milk samples closely align with those obtained in the test buffer (PBS), further validating the robustness of the device. The high recovery rates indicate minimal matrix interference, demonstrating the device's potential for real-world applications in food safety monitoring.

3. Conclusion

In this work, a dual-mode sensing platform was developed for the selective and ultrasensitive detection of ENF. The system combines magnetic-assisted extraction with electrochemical detection, offering both pre-concentration and signal transduction within a single 3D-printed miniaturized device. The synthesized MMIP, based on a magnetite core encapsulated within an APTES–TEOS–derived polymeric shell, demonstrated uniform core–shell morphology, optimized shell thickness (≈53 nm), and favorable surface characteristics for selective recognition. Structural characterization confirmed successful polymer formation, while nitrogen adsorption–desorption studies revealed enhanced surface area and mesoporous structure in the MMIP, ensuring improved analyte accessibility. Magnetic property evaluation confirmed that the MMIP retained sufficient magnetic responsiveness post-polymerization, essential for rapid external-field-driven separation.

The dual-mode nature of the sensing system, combining efficient magnetic-assisted target extraction with selective electrochemical detection, offers a significant operational advantage. This bifunctionality enables rapid assessment of ENF via magnetic isolation and direct signal transduction at the electrode interface, reducing the need for laborious sample pretreatment. Adsorption experiments established the superior binding performance of MMIP, with kinetic data fitting well to a pseudo-second-order model, suggesting chemisorption-dominated interaction. Equilibrium isotherms and Scatchard analyses revealed heterogeneous binding sites in MMIP with high- and low-affinity regions, while MNIP showed only non-specific binding. The calculated IF from adsorption (2.84) and electrochemical analysis (14.15) highlighted the enhancement achieved through electrochemical amplification. This significant increase is attributed not only to the broader dynamic detection range of the electrochemical platform but also to the synergistic effects of AuNPs and rGO, which markedly improved electron transfer, expanded electroactive surface area, and minimized charge transfer resistance. Their incorporation ensured heightened sensitivity and reproducibility in complex matrices.

Electrochemical evaluation using cyclic voltammetry (CV), electrochemical impedance spectroscopy (EIS), and differential pulse voltammetry (DPV) confirmed the successful stepwise electrode modification and demonstrated diffusion-controlled, stable, and high-performance sensing behavior. The fabricated MMIP/rGO/AuNP/WE sensor exhibited a wide linear detection range from 100 pM to 10 mM (10^{-10} to 10^{-2} M) with an ultralow detection limit of 161 fM (1.61×10^{-13} M). Selectivity assays against structural analogs and common interfering species confirmed the probe's target-specific response, while real sample testing in milk matrices demonstrated recovery rates between 90.23% and 97.29%, validating its practical applicability in food safety monitoring. Collectively, this work presents a robust sensing strategy combining molecular imprinting, magnetic separation, nanomaterial-enhanced electrochemical detection, and additive manufacturing. The integrated system offers a scalable, rapid, and field-deployable solution for trace-level monitoring of veterinary drug residues, with potential applicability in environmental surveillance and pharmaceutical quality control.

4. Experimental Section

Materials: All the chemicals and reagents used in this experiment were of high quality and purity. Enrofloxacin (ENF), Tetraethyl orthosilicate (TEOS), Ammonia solution ($NH_3 \bullet H_2O$), Iron (II) chloride tetrahydrate ($FeCl_2 \bullet 4H_2O$), and Iron (III) chloride hexahydrate ($FeCl_3 \bullet 6H_2O$) were procured from Sisco Research Laboratory Pvt. Ltd. (SRL), Mumbai, India. (3-Amonopropyl) triethoxysilane (APTES) was obtained from Sigma-Aldrich, Missouri, United States. Ethanol (C_2H_5OH), sodium hydroxide pellets (NaOH), Potassium Ferrocyanide hexacyanoferrate (II) trihydrate ($K_4[Fe(CN)_6] \bullet 3H_2O$), and Potassium Ferricyanide ($K_3[Fe(CN)_6]$) were obtained from HiMedia Laboratories, Mumbai, India. Methanol (CH_3OH) was procured from Merck, Massachusetts, United States. HCl was purchased from Qualigens Chemicals and Reagents, Thermo Fisher Scientific, Massachusetts, United States. Ciprofloxacin (CIP), Norfloxacin (NOR), and Ofloxacin (OFL) were obtained from a local drug store under the brand names Ciplox-500, Norflox-400, and OF-200 Ltd, respectively. Ciplox-500 and Norflox-400 were marketed by Cipla Ltd., Mumbai, India, and OF-200 was marketed by J.B. Chemicals and Pharmaceuticals Ltd., Mumbai, India. Industrial Grade Nitrogen (N_2 gas) was obtained from the local vendor in Varanasi, India. Milli Q water with a resistance of 18.2 MΩ•cm at 25 °C was obtained from Merck Millipore-based distillation unit, Massachusetts, United States.

Apparatus and Software: The electrochemical workstation used in this study was sourced from PalmSens BV, Houten, Netherlands,

supporting a three-electrode arrangement (Ag/AgCl reference, working electrode, and platinum (Pt) wire counter electrode). The morphological analysis of the synthesized MMIP was performed using a scanning electron microscope (EVO-Bench-top SEM MA15/18, Carl Zeiss AG, Germany) and a high-resolution transmission electron microscope (Tecnai G2 20 TWIN, FEI Company, United States). Magnetic properties were measured using a magnetic property measurement system (MPMS 3, SQUID-based magnetometer, Quantum Design Inc., United States). Physicochemical analyses were carried out using X-ray photoelectron spectroscopy (K-Alpha, Thermo Fisher Scientific, United States). Infrared spectra were recorded on a Fourier-transform infrared spectroscopy analyzer (Nicolet iS5, Thermo Electron Scientific Instruments LLC, United States). Surface area and porosity measurements were conducted using nitrogen adsorption–desorption analyzers (BELLSORP MAX II and BELCAT-II, MicrotracBEL Corp., Japan). UV-vis spectroscopy (Carry 60, Agilent Technologies Pvt Ltd, India) was used to confirm MMIP synthesis, template removal, and analyte binding. Printed electrodes were purchased from ItalSens IS-C (PalmSens BV, Houten, Netherlands). The magnetic assembly and ENF detection unit were designed using Blender software and 3D-printed on a Prusa Mini+ (Prusa Research, Czech Republic). Graphical representation and data analysis were performed using OriginPro 2021 (OriginLab Corporation, Massachusetts, USA).

Synthesis of the MMIP and MNIP: The synthesis of the MMIP involves consecutive steps that follow the preparation of the magnetite NPs, surface functionalization, molecular imprinting, and template removal (Scheme 2A). The magnetite NPs were synthesized by the co-precipitation method by dissolving 0.54 g of ferric chloride ($FeCl_3 \bullet 6H_2O$) and 0.20 g of ferrous chloride ($FeCl_2 \bullet 4H_2O$) in 50 mL of ultrapure Milli-Q water maintaining a molar ratio of 2:1 for the Fe^{3+} and Fe^{2+} ion. Then the whole solution setup was subjected to nitrogen purging to remove dissolved oxygen and to prevent oxidation of Fe^{2+} to Fe^{3+}. Following this, 2 M NaOH solution was added to it dropwise while raising the temperature to 90 °C and left under vigorous stirring for 1 h. The pH of the solution reaching ≈10 ensures complete precipitation of the dark black color. As the solution was cooled down to room temperature, it was washed multiple times using Milli-Q water and ethanol alternately to remove the excess solvents. Further, it was dried in an oven at 80 °C for 24 h, which led to the final magnetite NPs.

Following the synthesis of magnetite NPs, 100 mM ENF (template molecule) was mixed with 2 mL of APTES in 30 mL ethanol for 2 h to form a pre-polymerization solution. In a separate setup, 0.5 g of the magnetite NPs were dispersed in 100 mL of ethanol-water (2:1) and ultrasonicated for 30 mins. 25wt.% $NH_3 \bullet H_2O$ was added dropwise to this solution, followed by adding TEOS (2 mL), and left for continuous stirring for 0.5 h at 35 °C. For the final preparative step, the pre-polymerization solution was added dropwise to this, and the whole solution was stirred continuously for the next 1.5 h at room temperature. Then, it was washed multiple times using ethanol and water until the UV–vis absorption peak of ENF could not be detected in the supernatant. Consecutive MNIP was obtained similarly, except for the addition of the ENF as the template molecule. Template removal was performed by repeated washing of the polymer particles with methanol-acetic acid (9:1, v/v) as suggested in previous research,[59–61] until no residual enrofloxacin was detected, and the same protocol was applied to both MMIP and MNIP to ensure uniform post-synthetic treatment.

Characterization Methods: The synthesized MMIP and MNIP microparticles were characterized using complementary morphological, structural, textural, and magnetic analyses to validate their physical and chemical properties. For surface morphology assessment, SEM analysis was performed. Briefly, the dried MMIP and MNIP powders were mounted onto aluminum stubs using carbon adhesive tape and coated with a thin gold layer using a sputter coater to improve conductivity. SEM imaging was conducted using a ZEISS Sigma 300 scanning electron microscope operated at an accelerating voltage of 15 kV. The obtained micrographs were further analyzed using ImageJ software to determine particle size distribution. To investigate the internal structure and core–shell architecture, TEM analysis was carried out. A dilute suspension of MMIP or MNIP particles in ethanol was prepared by ultrasonication, and a small droplet was drop-cast onto a carbon-coated copper grid and allowed to dry at room temperature. TEM images and selected area electron diffraction (SAED) patterns were recorded using a JEOL JEM-2100 microscope operated at 200 kV. FTIR spectroscopy was used to confirm the surface functional groups and chemical composition of magnetite, MMIP, and MNIP. FTIR spectra were recorded using a FTIR spectrometer equipped with a diamond ATR accessory. Samples were scanned over the spectral range of 4000–400 cm^{-1} with a resolution of 4 cm^{-1}, and the spectra were averaged over 32 scans. Textural properties, including specific surface area, pore volume, and pore size distribution, were determined using nitrogen adsorption–desorption isotherms obtained on a BELLSORP MAX II and BELCAT-II analyzers (MicrotracBEL Corp., Japan). ≈100 mg of each sample was degassed at 120 °C under vacuum for 12 h prior to measurement. The Brunauer–Emmett–Teller (BET) method was employed to calculate surface area, while the Barrett–Joyner–Halenda (BJH) method was used to analyze the pore size distribution from the desorption isotherm. Magnetic measurements were performed to assess the magnetic characteristics of the synthesized materials. Dried samples were loaded into a nonmagnetic sample holder, and magnetization versus magnetic field (M–H) curves were measured at room temperature (300 K) using a Quantum Design magnetic property measurement system (MPMS). Measurements were performed over an applied field range of ±16 000 Oe to determine the saturation magnetization and evaluate the effect of polymer encapsulation on the magnetic behavior.

Adsorption Kinetics and Isotherm Study: Adsorption experiments were conducted to evaluate the binding characteristics of synthesized MMIP and MNIP toward ENF. Quantitative analysis was performed by monitoring the UV absorbance of ENF at 280 nm before and after incubation. The binding capacity of each microparticle was determined by calculating the decrease in ENF absorbance.

For kinetic studies, 10 mg of either MMIP or MNIP particles were dispersed in 10.0 mL of ENF solution (395.3 mg L^{-1}; 10 mM) prepared in a 2:3 (v/v) ethanol-PBS buffer (pH 7.4). The suspensions were incubated at ambient temperature under gentle shaking for varying time intervals (0 to 90 min). After each incubation period, the particles were magnetically separated, and the supernatant was filtered through a 0.22 µm membrane filter. The residual ENF concentration at time t (C_t, mg L^{-1}) was quantified using UV–visible spectrophotometry according to a previously reported method.[43] Thereafter, adsorption capacity at a given time (Q_t, mg g^{-1}) was calculated using Equation (1).

To construct adsorption isotherms, 10 mg of MMIP or MNIP was added to 10 mL of ENF standard solutions with varying initial concentrations (C_0, mg L^{-1} ranging in between 180 mg L^{-1} to 3594 mg L^{-1} (5×10^{-4} to 1×10^{-2} M) in the same ethanol-PBS buffer system. The suspensions were vortexed to achieve uniform dispersion and allowed to equilibrate for 35 min (t_e). After incubation, the polymers were magnetically separated, and the supernatant was filtered through a 0.22 µm membrane. The residual ENF concentration (C_e, mg L^{-1}) was measured spectrophotometrically, and the equilibrium adsorption capacity (Q_e, mg g^{-1}) was calculated using Equation (2).

Binding Mechanism and Intermolecular-Force Analysis: Template-free MMIP and MNIP powders (10 mg each) were dried at 60 °C for 12 h, spread onto a diamond ATR crystal (n = 32 scans), and baseline spectra were recorded. Each sample was then incubated with ENF (200 mg L^{-1}, pH 7.4) for 35 min, magnetically separated, rinsed twice with ethanol-PBS buffer (2:3, v/v), dried, and scanned again. The resulting shift in the spectrum ($\Delta A = A_{loaded} - A_{blank}$) was measured to highlight the interaction bands arising from ENF–polymer interactions. High- and low-affinity dissociation constants (K_d) and capacities (Q_m) were evaluated from the two linear regions of the Scatchard plot. Then the K_d values were converted to mol L^{-1} using the molar mass of ENF, i.e., 359.4 g mol^{-1}. Finally, the standard Gibbs free energy (ΔG°) was subsequently calculated with Equation (6).

Designing of the Sensor Probe: To design the final sensing probe conventional carbon electrode (WE) was primarily modified by electrodepositing the gold nanoparticles (AuNPs) employing a linear sweep voltammetry technique. As reported earlier,[46] a solution containing 0.001% $HAuCl_4$ in 0.5 M H_2SO_4 was taken to perform three consecutive

potential sweeps between +1.5 to +0.4 V (vs Ag/AgCl). An optimized step value of 0.001 V and a scan rate of 0.1 V s^{-1} was set, ensuring the deposition potential of −0.6 V (vs Ag/AgCl) and a deposition time of 60 s. This step is followed by thorough washing using Milli-Q water, leading to the formation of the AuNP/WE surface. Successively, rGO was coated onto the modified AuNPs/WE electrode from a 1 mg mL^{-1} stock concentration. This rGO was synthesized by chemically reducing Graphene Oxide (GO) using hydrazine hydrate as the reducing agent. Upon air drying, the coated AuNPs/WE were carefully washed using Milli-Q water to remove the unadsorbed/unbound rGO, which forms the rGO/AuNPs/WE.

The synthesized MMIP powder was used to prepare a suspension of 1 mg mL^{-1} in water from which 10 µL of MMIP was coated onto the modified rGO/AuNPs/WE surface and placed over a magnet to form the final sensing probe. During the detection of ENF, this 1 mg mL^{-1} suspension was prepared using the buffer (replacing water) containing ENF of a defined concentration. The probe is then subjected to washing and drying (keeping it over the magnet) at room temperature for the physicochemical adsorption of MMIP on the electrode surface, which leads to the formation of the final sensor probe MMIP/rGO/AuNPs/WE (Scheme 2B).

Electrochemical Studies: Electrochemical characterization and analytical measurements were carried out using a potentiostat system (PalmSens BV, Houten, Netherlands) integrated with a custom-designed electrochemical cell. All electrochemical experiments were conducted in phosphate-buffered saline (PBS, pH 7.0) containing 5 mM $[Fe(CN)_6]^{3-/4-}$ as the redox probe, unless otherwise specified. Cyclic voltammetry (CV) and electrochemical impedance spectroscopy (EIS) were performed to monitor the sequential modification of the working electrode (WE) surface, evaluate charge transfer properties, and assess the electrochemical stability of the sensor interface. CV measurements were recorded over a potential window of –0.6 to +0.9 V versus Ag/AgCl at a scan rate of 50 mV s^{-1}. EIS measurements were conducted across a frequency range of 0.01 Hz to 100 kHz using a 10-mV amplitude, and the impedance spectra were analyzed using a Randles equivalent circuit to extract the charge transfer resistance (R_{ct}).

DPV was employed to evaluate the analytical performance of the sensor, including ENF detection. DPV measurements were conducted in the potential range of +0.2 V to +1.0 V versus Ag/AgCl, with a pulse amplitude of 50 mV, a pulse width of 50 ms, and a scan rate of 10 mV s^{-1}. Calibration studies were performed by testing the MMIP/rGO/AuNP/WE sensor in ENF solutions with concentrations ranging from 10^{-10} to 10^{-2} M, and the corresponding current responses were recorded.

Selectivity experiments were conducted using potential interfering compounds commonly present in milk samples, including glucose, lactose, ascorbic acid, urea, casein, L-histidine, L-methionine, thiamine, and niacinamide. To further evaluate molecular selectivity and anti-interference performance, structurally related fluoroquinolone antibiotics, i.e., CIP, NOR, and OFL, were included in the selectivity assessment. These commercial drug tablets were used to calculate the required mass for solution preparation. Each tablet was finely crushed, dissolved in deionized water, and filtered through a 0.22 µm membrane to remove insoluble excipients. Stock solutions were then diluted to a final concentration of 1 µM. For incubation, 1 mL of each prepared fluoroquinolone solution was mixed with 1 mg of MMIP or MNIP microparticles in microtubes, vortexed briefly for uniform dispersion, and incubated at room temperature (25 °C) for 35 min under gentle shaking to promote analyte–polymer interactions. After incubation, magnetic separation was employed to collect the microparticles, followed by two washing steps with PBS (pH 7.4) to remove unbound species. The washed microparticles were then deposited onto the modified sensor chips for subsequent DPV measurements to assess current responses and evaluate interference effects.

All electrochemical measurements were conducted in triplicate ($n = 3$) to ensure reproducibility. Whereas, the selectivity assays are performed in quintuplicate ($n = 5$). Results were interpreted in conjunction with the structural and adsorption characterization data to correlate sensor performance with material properties.

Supporting Information

Supporting Information is available from the Wiley Online Library or from the author.

Acknowledgements

SM acknowledges the DST INSPIRE [IF170804], Government of India, fellowship for providing research support. AS [File no: 09/1217(17501)/2024-EMR-I] acknowledges the Council of Scientific and Industrial Research (CSIR) for providing financial support. The authors also thank the Central Instrument Facility Center (CIFC), and IIT (BHU) Varanasi for providing the SEM, TEM, XPS, FTIR, BET, and MPMS facilities. Licenses for the Origin software and the Microsoft platforms (Office and Clipchamp) were provided by IIT (BHU) Varanasi. Graphics were generated using Blender, an open-source 3D computer graphics software tool, and Microsoft PowerPoint.

Conflict of Interest

The authors declare no conflict of interest.

Data Availability Statement

The data that support the findings of this study are available from the corresponding author upon reasonable request.

Keywords

3D-printed sensing platform, electrochemical sensor, enrofloxacin detection, magnetic molecularly imprinted polymer, miniaturized device

Received: March 5, 2025
Revised: May 13, 2025
Published online: June 27, 2025

[1] Y. Zou, Z. Sun, Q. Wang, Y. Ju, N. Sun, Q. Yue, Y. Deng, S. Liu, S. Yang, Z. Wang, F. Li, Y. Hou, C. Deng, D. Ling, Y. Deng, *Chem. Rev.* **2025**, *125*, 972.
[2] R. Campanile, V. C. Elia, A. Minopoli, Z. Ud Din Babar, R. d Girolamo, A. Morone, N. Sakač, R. Velotta, B. Della Ventura, V. Iannotti, *Talanta* **2023**, *253*, 123937.
[3] M. R. Rather, S. Abass, S. Jahan, K. Sultan, R. Samad, *J. Magn. Magn. Mater.* **2024**, *596*, 171994.
[4] E. G. Fuller, H. Sun, R. D. Dhavalikar, M. Unni, G. M. Scheutz, B. S. Sumerlin, C. Rinaldi, *ACS Appl. Polym. Mater* **2019**, *1*, 211.
[5] R. Jenjob, T. Phakkeeree, D. Crespy, *Biomater. Sci.* **2020**, *8*, 2756.
[6] F. M. Galogahi, Y. Zhu, H. An, N. T. Nguyen, *J. Sci.: Adv. Mater. Devices* **2020**, *5*, 417.
[7] M. Nedylakova, J. Medinger, G. Mirabello, M. Lattuada, *Adv. Colloid Interface Sci.* **2024**, *323*, 103056.
[8] B. D. Cullity, C. D. Graham, *Introduction to Magnetic Materials*, Wiley, Hoboken, New Jersey, USA, **2008**, https://onlinelibrary.wiley.com/doi/book/10.1002/9780470386323.
[9] H. Shokrollahi, *J. Magn. Magn. Mater.* **2017**, *426*, 74.
[10] E. P. Plueddemann, *Silane Coupling Agents*, Springer US, New York, NY, **1991**, https://link.springer.com/book/10.1007/978-1-4899-2070-6.
[11] M. Peng, S. Salaheen, D. Biswas, in *Encyclopedia of Agriculture and Food Systems*, Elsevier, Amsterdam, **2014**, pp. 346–357.

[12] T. Trouchon, S. Lefebvre, *Open J. Vet. Med.* **2016**, *06*, 40.
[13] Official Journal of European Union, L15 **2010**, pp. 1–72, https://eur-lex.europa.eu/LexUriServ/LexUriServ.do?uri=OJ:L:2010:015:0001:0072:en:PDF.
[14] J. Dai, Y. Wang, H. Lin, Y. Sun, Y. Pan, J. qin Qiao, H. zhen Lian, C. xiang Xu, *Food Chem.* **2023**, *404*, 134757.
[15] L. Lucatello, P. Cagnardi, F. Capolongo, C. Ferraresi, F. Bernardi, C. Montesissa, *Food Control* **2015**, *48*, 2.
[16] D. Arslan-Acaröz, N. B. Sözbilir, *Ankara Univ. Vet. Fak. Derg.* **2020**, *67*, 137.
[17] S. Wu, J. Mao, Y. Zhang, S. Wang, M. Huo, H. Guo, *Food Chem.* **2023**, *413*, 135579.
[18] E. Bakker, M. Telting-Diaz, *Anal. Chem.* **2002**, *74*, 2781.
[19] B. Purohit, P. R. Vernekar, N. P. Shetti, P. Chandra, *Sens. Int.* **2020**, *1*, 100040.
[20] C. Zhu, G. Yang, H. Li, D. Du, Y. Lin, *Anal. Chem.* **2015**, *87*, 230.
[21] S. Lu, S. Wang, P. Wu, D. Wang, J. Yi, L. Li, P. Ding, H. Pan, *Adv. Powder Technol.* **2021**, *32*, 2106.
[22] L. Yuting, Z. Jing, L. Donghui, *Chirality* **2019**, *31*, 23045.
[23] B. G. Fouda-Mbanga, O. P. Onotu, Z. Tywabi-Ngeva, *Green Anal. Chem.* **2024**, *11*, 100156.
[24] Q. Yu, H. Yang, Y. Yang, *J. Food Measure. Charact.* **2024**, *18*, 87.
[25] O. Sadak, *Nanocomposites* **2021**, *7*, 44.
[26] X. Su, X. Tian, Z. Sun, X. Zou, W. Zhang, *Microchem. J.* **2023**, *190*, 108576.
[27] K. Mahato, B. Purohit, K. Bhardwaj, A. Jaiswal, P. Chandra, *Biosens. Bioelectron.* **2019**, *142*, 111502.
[28] U. P. Azad, P. Chandra, *Handbook of Nanobioelectrochemistry: Application in Devices and Biomolecular Sensing*, Springer, Singapore, **2023**.
[29] B. Purohit, P. Chandra, *Surface Engineering and Functional Nanomaterials for Point-of-Care Analytical Devices*, Springer, Singapore, **2023**.
[30] S. N. Joshi, P. Chandra, *Advanced Micro- and Nano-Manufacturing Technologies*, Springer, Singapore, **2022**.
[31] P. Sivolapov, O. Myronyuk, D. Baklan, *Inorg. Chem. Commun.* **2022**, *143*, 109769.
[32] S. L. Greasley, S. J. Page, S. Sirovica, S. Chen, R. A. Martin, A. Riveiro, J. V. Hanna, A. E. Porter, J. R. Jones, *J. Colloid Interface Sci.* **2016**, *469*, 213.
[33] M. Maccario, L. Croguennec, A. Wattiaux, E. Suard, F. Le Cras, C. Delmas, *Solid State Ion* **2008**, *179*, 2020.
[34] S. Gallis, V. Nikas, A. E. Kaloyeros, in *Modern Technologies for Creating the Thin-Film Systems and Coatings*, InTech, London, UK, **2017**.
[35] N. S. da Silva, A. C. Alves, J. A. da Silva Pereira, L. A. de Oliveira, M. C. L. de Oliveira, R. A. Antunes, *Metals (Basel)* **2024**, *14*, 1019.
[36] H. He, Y. Hu, S. Chen, L. Zhuang, B. Ma, Q. Wu, *Sci. Rep.* **2017**, *7*, 3913.
[37] K. S. W. Sing, R. T. Williams, *Adsorpt. Sci. Technol.* **2004**, *22*, 773.
[38] G. Xiong, B. Bin Wang, L. X. You, B. Y. Ren, Y. K. He, F. Ding, I. Dragutan, V. Dragutan, Y. G. Sun, *J. Mater. Chem.: A Mater.* **2019**, *7*, 393.
[39] E. D. Revellame, D. L. Fortela, W. Sharp, R. Hernandez, M. E. Zappi, *Clean Eng. Technol.* **2020**, *1*, 100032.
[40] D. Robati, *J. Nanostruct. Chem.* **2013**, *3*, 55.
[41] L. Hajiaghababaei, A. Mazloomifar, F. Khalilian, G. T. Farahani, *Sci. Rep.* **2025**, *15*, 5905.
[42] A. Banchhor, M. Pandey, P. K. Pandey, *Water Conserv. Sci. Eng.* **2021**, *6*, 127.
[43] H. T. Nguyen, N. T. Vuong Bui, W. G. Kanhounnon, K. L. Vu Huynh, T. V. A. Nguyen, H. M. Nguyen, M. H. Do, M. Badawi, U. D. Thach, *RSC Adv.* **2021**, *11*, 34281.
[44] N. S. Myshakina, Z. Ahmed, S. A. Asher, *J. Phys. Chem. B.* **2008**, *112*, 11873.
[45] P. A. Borea, K. Varani, S. Gessi, P. Gilli, A. Dalpiaz, *Il Farmaco* **1998**, *53*, 249.
[46] S. Mahapatra, P. Chandra, *ACS Sustainable Chem. Eng.* **2023**, *11*, 17249.
[47] T. N. Q. Do, T. T. H. Vu, Q. H. Le, T. P. N. Pham, T. T. Ta, T. L. Nguyen, T. H. Y. Pham, *Anal. Lett.* **2024**, *57*, 1989.
[48] M. Antilén, C. Valencia, E. Peralta, C. Canales, C. Espinosa-Bustos, M. Escudey, *Electrochim. Acta.* **2017**, *244*, 104.
[49] N. Karuppusamy, V. Mariyappan, S. M. Chen, R. Ramachandran, *Nanoscale* **2022**, *14*, 1250.
[50] F. Gagliani, T. Di Giulio, S. Grecchi, T. Benincori, S. Arnaboldi, C. Malitesta, E. Mazzotta, *Molecules* **2024**, *29*, 1632.
[51] F. Dönmez, Y. Yardım, Z. Şentürk, *Diamond Relat. Mater.* **2018**, *84*, 95.
[52] C. Canales, E. Peralta, M. Antilen, *J. Electroanal. Chem.* **2019**, *832*, 329.
[53] C. Yan, R. Zhang, Y. Chen, G. Wang, *J. Electroanal. Chem.* **2017**, *806*, 130.
[54] S. S. Khaloo, S. Mozaffari, A. Barekat, F. Karimi, *Micro Nano Lett.* **2015**, *10*, 476.
[55] A. A. Ensafi, M. Taei, T. Khayamian, F. Hasanpour, *Anal. Sci.* **2010**, *26*, 803.
[56] X. Si, Y. Wei, C. Wang, L. Li, Y. Ding, *Anal. Methods* **2018**, *10*, 1961.
[57] Y. Fu, Y. Xie, H. Shi, G. Zhang, H. Zhang, S. Feng, *Food Chem.* **2023**, *429*, 136921.
[58] B. Shen, X. Wen, G. V. Korshin, *Environ. Sci. Process Impacts* **2018**, *20*, 943.
[59] R. A. Lorenzo, A. M. Carro, C. Alvarez-Lorenzo, A. Concheiro, *Int. J. Mol. Sci.* **2011**, *12*, 4327.
[60] X. Wang, Y. Zhou, Y. Niu, S. Zhao, B. Gong, *Int. J. Anal. Chem.* **2019**.
[61] Z. Sun, H. Liu, Y. Zhou, S. Zhao, J. Li, X. Wang, B. Gong, *RSC Adv.* **2019**, *9*, 27953.